J. Fluid Mech. (2011), *vol.* 672, *pp.* 487–520.
doi:10.1017/S0022112010006130

Viscous–inviscid interactions in transonic flows through slender nozzles

A. KLUWICK† AND G. MEYER

Institute of Fluid Mechanics and Heat Transfer, Vienna University of Technology, Resselgasse 3/322, 1040 Vienna, Austria

(Received 5 May 2010; revised 23 September 2010; accepted 22 November 2010; first published online 18 February 2011)

Considering the miniaturization trend in technical applications, the need of a slender nozzle theory for such conventional, that is ideal-gas-like, fluids, which accounts for a strong boundary-layer interaction with the core region, arises in quite a natural way as the dimensions of the flow device are successively reduced. Moreover, a number of modern technological processes (e.g. organic Rankine cycles) involve fluids with high molecular complexity, some of which are expected to exhibit embedded regions with negative values of the fundamental derivative in the vapour phase commonly termed Bethe–Zel'dovich–Thompson (BZT) fluids. Linked to it, unconventional Laval nozzle geometries are needed to transform subsonic to supersonic internal flows. In the present paper, the transonic flows through nozzles of short length scales located in a channel of constant cross-section so slender that the flow in the inviscid core region is one-dimensional are considered. Rapid streamwise changes of the flow field caused by the nozzle then lead to a local breakdown of the classical hierarchical boundary-layer approach, which is overcome by the triple-deck concept. Consequently, the properties of the inviscid core and the near-wall (laminar) boundary-layer regions have to be calculated simultaneously. The resulting problem is formulated for both regular (ideal-gas-like) fluids and dense gases. Differences and similarities of the resulting flow pattern with respect to the well-known classical Laval nozzle flow are presented for perfect gases, and the regularizing influence of viscous–inviscid interactions, is examined. Furthermore, the analogous problem is considered for BZT fluids in detail as well. The results indicate that the passage through the sonic point in the inviscid core is strongly affected by the combined influence of nozzle geometry and boundary-layer displacement effects suggesting in turn an inverse Laval nozzle design in order to obtain the desired flow behaviour.

Key words: boundary layers, complex fluids, compressible flows

1. Introduction

In the preceding paper Kluwick & Meyer (2010), we have considered the influence of viscous–inviscid interactions on the transition of fluids in the vapour phase from supersonic to subsonic flow via weak normal shocks in a channel of a constant cross-section. The channel has been assumed to be so slender that the (laminar) boundary layer correction at the walls for high Reynolds numbers can no longer be considered to be an effect of higher order, but rather has to be considered at leading order in

† Email address for correspondence: alfred.kluwick@tuwien.ac.at

the framework of a triple-deck theory. Moreover, the inviscid core region flow, which is confined within the two interacting boundary layers at the channel walls, has been required to be one-dimensional to leading order. As a direct consequence of the strong shock–boundary layer interaction in slender channels, a normal shock is transformed into a smooth pseudo-shock; cf. Kluwick & Meyer (2010). The regularizing mechanism of viscous–inviscid interactions in internal flows has been found to be quite different from the well-known thermo–viscous regularization in connection with external flows. The interacting boundary layers form a kind of viscous nozzle which interacts with and at the same time reacts to the induced pressure perturbations in the inviscid core. The focus of the aforementioned study has been to gain theoretical insight into shock regularization of conventional shocks (compression shocks) and non-conventional types of shocks (e.g. rarefaction shocks) in the vapour phase without undergoing phase transition. The latter shock types are, however, only possible for a limited class of fluids consisting of complex molecules known as dense gases or Bethe–Zel'dovich–Thompson (BZT) fluids; e.g. Cramer (1991). This is true at least from a theoretical point of view, as an experimental verification of the proclaimed non-conventional thermodynamic behaviour eludes experimental verification as yet and is currently an active field of research (cf. e.g. Fergason *et al.* 2001; Guardone, Zamfirescu & Colonna 2010). Presently, the experimental detection of such reported dense gas behaviour relies on variants of shock-tube experiments, cf. Guardone *et al.* (2010). In Kluwick & Meyer (2010), we have argued that the observation of pseudo-shocks in a slender channel could propose an interesting alternative experimental set-up to shock-tube experiments. An obvious advantage of a stationary set-up is that it avoids complicated irregular wave patterns caused by the rupture of the diaphragm, which can be eliminated only by the use extremely fast opening valves. A major drawback, however, would be that the shock position in a channel of a constant cross-section is unfortunately very sensitive to perturbations. An extension of the theory presented before to slender nozzles, which is the aim of the present paper, provides an elegant way to control the actual shock position by the nozzle design and thereby reduce its sensitivity to perturbations. Of course, the sensibility of the flow phenomena with respect to various other sources, such as variations of thermodynamic conditions and boundary conditions, is not reduced, since these are problem-inherent and a consequence of the extremely small inversion zone in real gases, where rarefaction shocks are possible.

Besides the fundamental question of the existence of rarefaction shocks in the vapour phase, the unconventional behaviour of BZT fluids opens up some interesting possibilities for technical applications, especially as working media in organic Rankine thermal power cycles; cf. e.g. Cinnella & Congedo (2007) or Brown & Argrow (2000). Because of the relatively small values of the speed of sound of dense gases close to the thermodynamical critical point, there arises the need to convert subsonic flows to the supersonic regime by means of a nozzle. However, taking a look at the estimates on the actual dimensions of the interaction region and the appropriate channel heights performed in Kluwick & Meyer (2010) for the example fluid PP10 ($C_{13}F_{22}$) with possible BZT fluid character reveals that the reported flow phenomena of viscous–inviscid interactions are likely to be encountered in such flow devices for dense gases of quite realistic technical dimensions. Consequently, the implications of a strong boundary layer interaction with the inviscid core region flow again may not be neglected in the construction of flow devices, unlike in conventional nozzle design.

Taking into account the trend in technical applications towards miniaturization, the need of a nozzle theory, in which the strong boundary layer interaction with the core region has to be accounted for, arises in quite a natural way as the dimensions

of the flow device are successively reduced. To the authors' knowledge, such a theory has not been formulated so far even for perfect gases which at present are of more importance as far as practical applications are concerned. The investigation of the regular perfect-gas-like fluid behaviour, therefore, serves as the natural starting point for a discussion of flows through slender nozzles in §4.2.1 and in particular the consequences of viscous–inviscid interactions, since the results of the purely inviscid one-dimensional Laval nozzle theory for perfect gas are readily at hand and widely known, see for example Oswatitsch (1956).

Therefore, in the present paper, we aim to investigate the conversion of subsonic to supersonic high-Reynolds-number flows by means of a small nozzle located in a slender channel of an otherwise constant cross-section, both for regular fluids and dense gases, which are characterized by the fundamental derivative of gasdynamics defined as

$$\Gamma = \frac{1}{\tilde{c}} \frac{\partial(\tilde{\rho}\tilde{c})}{\partial \tilde{\rho}}\bigg|_{\tilde{s}} \tag{1.1}$$

introducing the speed of sound

$$\tilde{c} = \sqrt{\left(\frac{\partial \tilde{p}}{\partial \tilde{\rho}}\right)_{\tilde{s}}}, \tag{1.2}$$

the thermodynamic pressure $\tilde{p}$, the density $\tilde{\rho}$ and the specific entropy $\tilde{s}$. In the following, we refer to fluids as regular fluids if the fundamental derivative is positive in the entire flow field considered and as a dense gas if the fundamental derivative is negative or changes its sign. The prototype of a regular fluid is, of course, a perfect gas where Γ is a positive constant $\Gamma = (\kappa+1)/2$, where κ denotes the ratio of specific heats.

The resulting boundary-layer interaction problem will be formulated for transonic internal flows by means of matched asymptotic expansions exploiting the largeness of the Reynolds number. For this purpose, the geometrical configuration of a small surface-mounted hump at the lower and upper channel walls forming a short nozzle in a narrow channel as depicted in figure 1 will be considered. At high Reynolds numbers, viscous effects near the channel inlet are limited to thin layers adjacent to the channel walls, and Prandtl's classical boundary layer theory for laminar flow provides a good description of the resulting flow (except for a tiny region near the leading edge where the full Navier–Stokes equations apply as in the case of external flows), in general. Yet, the boundary layer correction affects only the inviscid core-region flow in higher orders, and therefore the core-region flow regime and the boundary layer flow are interlinked in a strictly hierarchical way excluding a strong interaction. However, the rapid changes in the streamwise direction which are introduced by the short nozzle (possibly in connection with a pseudo-shock, cf. figure 1) lead to a local breakdown of the classical boundary layer approach; cf. Stewartson (1974) or Kluwick (1998). As a direct consequence, the properties of the inviscid core and the viscosity-dominated boundary layer regions can no longer be determined in subsequent steps but have to be calculated simultaneously within an asymptotically small interaction region around the nozzle depicted by region 3 in figure 1. The interaction problem will be formulated in terms of a triple-deck problem (cf. Stewartson 1974), where the inviscid interacting core region is represented by a single upper deck which is shared by the two interacting boundary layers at the lower and upper channel walls. The interacting boundary layer itself is subdivided into an asymptotically thin lower-deck accounting for wall-near effects of viscosity and a passive main deck comprising the main part

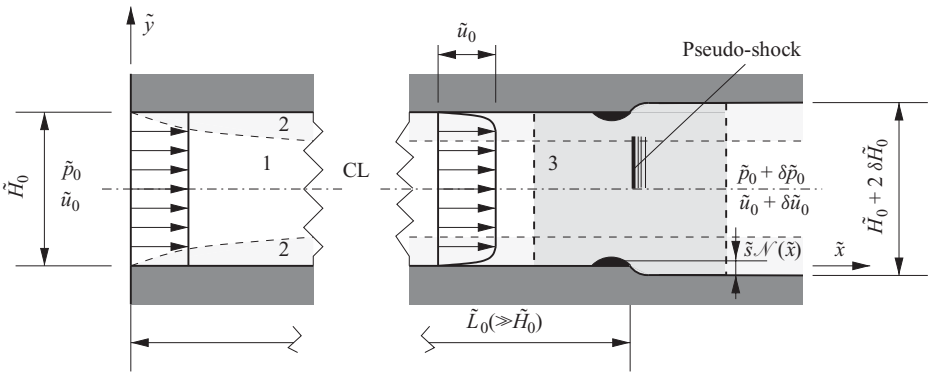

FIGURE 1. Schematic sketch of the problem set-up. Region 1, inviscid core; region 2, viscous non-interacting boundary layers; region 3, viscous–inviscid interaction; CL, centreline.

of the interacting boundary layer. As in the study of Kluwick & Meyer (2010), the channel shall be sufficiently narrow so that the flow in the inviscid core becomes one-dimensional to the leading order. Correspondingly, the present work can be seen as an extension to the above paper as well as to the study on one-dimensional purely inviscid internal flows of dense gases through nozzles outlined by Kluwick (1993).

It is the aim – both of the preceding and the present paper – to provide insight into the fundamental mechanism of interacting regular and dense gas flows which rest on a firm theoretical basis relying on matched asymptotic expansions. At present, this can only be achieved for the case of laminar flow, since a similarly rigorous treatment of turbulent flows does not appear to be possible at the moment. Of course, considerations of the limit Reynolds number to infinity are, strictly speaking, not compatible with the assumption of laminar flow. However, there is a reason to hope that the results obtained in this limit are at least qualitatively correct for high-Reynolds-number laminar flows satisfying the proposed scalings as has been found in other triple-deck studies, see for example Stewartson (1981). This, however, can in the end only be validated by experiments.

This paper is structured as follows. Suitable reference states for the various quantities relevant to the problem set-up and the governing equations in dimensionless form are introduced in § 2. In § 2.1, we briefly describe the magnitude of the various dimensional groups entering the governing equations (presented in § 2 of Kluwick & Meyer 2010). The formulation of the fundamental problem together with the asymptotic analysis is given in §§ 3.1 and 3.2, and important asymptotic properties of solutions to the fundamental problem are discussed in §§ 3.3 and 3.4. Finally, numerical solutions are presented in § 4. The numerical method is outlined in § 4.1. Section 4.2 discusses the steady flow field in nozzles of similar shape but varying minimal throat area for regular fluids (§ 4.2.1) and varying maximal throat area for dense gases having $\Gamma < 0$ in the entire flow regime to be considered (§ 4.2.2). Sections 4.2.1 and 4.2.2 discuss the differences and similarities to conventional purely inviscid and one-dimensional Laval nozzle flows. The last section (§ 4.3) deals with the calculation of nozzle shapes required to generate a certain desired pressure distribution in terms of an inverse problem formulation for both regular fluids and dense gases, where Γ now is not restricted to sole negative values, but can change sign in the flow field.

2. Problem formulation I: governing equations

Analogous to the problem of shock-wave regularization by viscous–inviscid interactions in a slender channel discussed in Kluwick & Meyer (2010), we introduce the non-dimensional quantities (tilde denotes dimensional quantities) in the following way:

$$\left.\begin{gathered}(\tilde{x},\tilde{y})=\tilde{L}_0(x,y),\quad (\tilde{u},\tilde{v})=\tilde{u}_0(u,v),\quad \tilde{t}=\frac{\tilde{L}_0}{\tilde{u}_0}\,t,\quad \tilde{H}_0=\tilde{L}_0H_0,\quad \tilde{s}_{\mathscr{N}}=\tilde{L}_0 s_{\mathscr{N}},\\ \tilde{p}=\tilde{\rho}_0\tilde{u}_0^2\,p,\quad \tilde{\rho}=\tilde{\rho}_0\,\rho,\quad \tilde{c}=\tilde{c}_0\,c,\quad \tilde{\theta}=\tilde{\theta}_0\,\theta,\quad \tilde{h}=\tilde{u}_0^2\,h,\\ \tilde{s}=\tilde{c}_{p,0}s,\quad \tilde{\mu}=\tilde{\mu}_0\,\mu,\quad \tilde{\mu}_b=\tilde{\mu}_0\,\mu_b,\quad \tilde{k}=\tilde{k}_0\,k.\end{gathered}\right\}\tag{2.1}$$

Here $(\tilde{x},\tilde{y})$ denote coordinates in the horizontal and vertical directions, $(\tilde{u},\tilde{v})$ are the corresponding components of the velocity vector, $\tilde{t}$ is the time, $\tilde{H}_0$ is the channel height at the entry, $\tilde{s}_{\mathscr{N}}$ is the contour of the nozzle, $\tilde{c}$ is the speed of sound, $\tilde{\rho}$ is the density, $\tilde{p}$ is the pressure, $\tilde{\theta}$ is the temperature, $\tilde{h}$ is the specific enthalpy, $\tilde{s}$ is the specific entropy, $\tilde{c}_p$ is the specific heat capacity at constant pressure, $\tilde{\mu}$ is the dynamic viscosity, $\tilde{\mu}_b$ is the bulk viscosity, and $\tilde{k}$ is the thermal conductivity. The subscript 0 indicates a reference state characterizing the inlet conditions and the undisturbed core region upstream of the interaction region as well. The interaction process itself is evoked by the presence of a nozzle of a given shape $\tilde{s}_{\mathscr{N}}(x)$, cf. figure 1. The nozzle is of short length scales, which in turn introduces rapid changes within the streamwise flow field and thus triggers the viscous–inviscid interaction process. It is located in the channel at a distance $\tilde{L}_0$ from the entry; consequently, the variation of the area of cross-section is restricted to a short region around $\tilde{L}_0$ and $\partial_{\tilde{x}}\tilde{s}_{\mathscr{N}}(x)=0$ upstream and downstream of the interaction region. Therefore,

$$\tilde{s}_{\mathscr{N}}(\tilde{x})=0, \qquad \text{upstream of interaction region,} \tag{2.2}$$

$$|\tilde{s}_{\mathscr{N}}(\tilde{x})|=\delta\tilde{H}_0, \qquad \text{downstream of interaction region.} \tag{2.3}$$

In contrast to the meaning of $\delta\tilde{H}_0$, $\delta\tilde{u}_0$, $\delta\tilde{\rho}_0$ and $\delta\tilde{p}_0$ given in Kluwick & Meyer (2010), these quantities are not associated with small variations of the flow conditions at the inlet with respect to the reference state but rather denote the small variations of the channel height and the flow conditions caused by the nozzle $\tilde{s}_{\mathscr{N}}$ far downstream the interaction region, cf. figure 1.

In terms of the non-dimensional quantities (2.1), the Navier–Stokes equations for two-dimensional compressible flows neglecting gravitational forces can be written as

$$\frac{\partial\rho}{\partial t}+\partial_i(\rho u_i)=0, \tag{2.4a}$$

$$\rho\left(\frac{\partial u_i}{\partial t}+u_j\partial_j u_i\right)=-\partial_i p+\frac{1}{Re}\,\partial_j\tau_{ij}, \tag{2.4b}$$

$$\frac{c^2}{M_0^2}\frac{\mathrm{D}\rho}{\mathrm{D}t}-\frac{\mathrm{D}p}{\mathrm{D}t}=\frac{G_0\bar{G}}{Re}\left(\tau_{ij}\partial_j u_i+\frac{1}{PrEc}\,\partial_k(k\,\partial_k\theta)\right), \tag{2.4c}$$

with the stress tensor for a Newtonian fluid $\tau_{ij}=\mu_b\partial_k u_k\delta_{ij}+\mu(\partial_j u_i+\partial_i u_j-\frac{2}{3}\partial_k u_k\delta_{ij})$ and the substantial derivative $\mathrm{D}(\cdot)/\mathrm{D}t$. The resulting dimensionless groups

$$Re:=\frac{\tilde{\rho}_0\tilde{L}_0}{\tilde{\mu}_0},\quad M_0:=\frac{\tilde{u}_0}{\tilde{c}_0},\quad Ec:=\frac{\tilde{u}_0^2}{\tilde{c}_{p,0}\tilde{T}_0},\quad Pr:=\frac{\tilde{k}_0}{\tilde{\mu}_0\tilde{c}_{p,0}},\quad G_0:=\frac{\tilde{\rho}_0}{\tilde{\theta}_0}\left(\frac{\partial\tilde{\theta}}{\partial\tilde{\rho}}\right)_{\tilde{s},0} \tag{2.5}$$

	Regular fluid	Dense gas
Re	$\gg 1$	$\gg 1$
M_0	≈ 1	≈ 1
Ec	$O(1)$	$\ll 1$
Pr	$O(1)$	$O(1)$
G_0	$O(1)$	$\ll 1$

TABLE 1. Assumptions on the order of magnitude for the relevant dimensionless groups.

denote the Reynolds, the Mach, the Eckert, the Prandtl numbers and the Grüneisen coefficient G evaluated at the reference state, respectively. Here $\bar{G} = G/G_0 = O(1)$ entering (2.4c) then denotes a properly scaled Grüneisen coefficient. For later convenience, we introduce the quantity

$$\bar{c} := c/M_0 = \tilde{c}/\tilde{u}_0. \tag{2.6}$$

The centreline of the nozzle $y = H_0/2$ (and labelled CL in figure 1) is a line of symmetry along which

$$\frac{\partial u}{\partial y} = \frac{\partial p}{\partial y} = 0, \quad x > 0, \quad y = \frac{H_0}{2}; \tag{2.7}$$

consequently, it is sufficient to specify the boundary conditions for the lower half-plane only. The boundary conditions at the (adiabatic) wall are

$$(u, v) = (0, 0), \quad \frac{\partial \theta}{\partial y} = 0, \quad x > 0, \quad y = s_{\mathscr{W}}(x). \tag{2.8}$$

The undisturbed state $(\tilde{u}, \tilde{v}) = \tilde{u}_0(1, 0)$, $\tilde{\rho} = \tilde{\rho}_0$ and $\tilde{p} = \tilde{p}_0 = \tilde{\rho}_0 \tilde{u}_0^2$ p_0 is taken to hold at the channel entry, i.e.

$$(u, v) = (1, 0), \quad \rho = 1, \quad p = p_0, \quad x = 0, \quad 0 < y < H_0. \tag{2.9}$$

2.1. *Order-of-magnitude estimates of dimensionless groups*

Table 1 summarizes the physical setting of interest by stating the orders of magnitude we require of the dimensionless groups (2.5). In Kluwick & Meyer (2010), the implications of these assumptions have been discussed in detail; here we only mention the important arguments for the sake of completeness. Briefly, the requirements $Re \gg 1$ and $M_0 \approx 1$ concern the characterisation of the flow regime in which the theory is applicable, whereas the estimates of Ec, Pr and G_0 concern the thermodynamic properties of the class of fluids considered under such flow conditions. Specifically, we note that the smallness of G_0 for dense gases simply expresses the fact that isotherms and isentropes tend to coincide when the fluid specific heats tend to infinity, that is become large.

Most importantly, the condition $Re \gg 1$ leads to the formation of viscosity-dominated boundary layers near the channel walls. The assumption of transonic flow, $M_0 \approx 1$, allows the study of weak transitions from supersonic to subsonic flow conditions (and *vice versa*) by means of an asymptotic theory.

The thermodynamic region of interest is restricted to the single-phase gas regime. Dense gas behaviour associated with a change of sign of the fundamental derivative Γ can be expected for various classes of fluids of higher molecular complexity

(Cramer 1991), and then occurs only in a relatively small region in the vicinity of the thermodynamical critical point which is located above the region of gas-vapour coexistence in the p- versus $1/\rho$-diagram (see figure 2*a*; Kluwick 2004). In the following, we refer to a fluid as being regular if the fundamental derivative is positive and the reference state is sufficiently far away from the transition line $\Gamma = 0$, so that the fluid is not supposed to access the region of negative Γ within the entire flow field under flow conditions to be considered, and we refer to a fluid as exhibiting dense gas behaviour otherwise. The present theory is applicable in both thermodynamic regimes.

3. Problem formulation II: interaction problem

3.1. *Preliminary remarks on the core flow region*

3.1.1. *One-dimensional transonic flow in channel core*

As has been pointed out in the Introduction, we impose an additional order-of-magnitude constraint which is not based on the inspection of the dimensionless groups in the governing equations, namely the condition of a narrow channel $H_0/L_0 \ll 1$. More precisely, the channel height H_0 shall depend on the limiting procedure in such a way that the compressible, inviscid flow in the core region, i.e. upper deck, of the interaction region becomes one-dimensional to leading order as $Re \to \infty$. The appropriate choice of the Re number dependency of H_0 has been found by employing an inspection analysis; cf. Kluwick & Meyer (2010) for details. There, the compatibility relations along right- and left-running characteristics have been used as the starting point of the inspection analysis of the upper-deck flow regime. The local reduction of the area of cross-section within the interaction region has been related to the perturbation of the displacement thickness, as seen in figure 3, which captures the displacement effect exerted by the interacting boundary layers at the channel walls on the inviscid core. An inspection of the compatibility relations is useful in revealing the relevant physical mechanism associated with viscous–inviscid interactions in slender channels and determining the choice of time scaling associated with the long-term behaviour of the system on the basis of the characteristic wave speeds. However, it is worthwhile noting that the distinguished limit obtained for the upper-deck problem can, of course, also be derived by considering the full (two-dimensional) Navier–Stokes equations (2.4*a*)–(2.4*c*). To this end, by means of (2.4*b*) and (2.4*a*), respectively, the substantial derivative of the pressure and the density is rewritten as

$$\frac{\mathrm{D}p}{\mathrm{D}t} = \frac{\partial p}{\partial t} + u_i \partial_i p = \frac{\partial p}{\partial t} + u_i \left(-\rho \frac{\partial u_i}{\partial t} - \rho u_j \partial_j u_i + \frac{1}{Re} \partial_j \tau_{ij} \right), \tag{3.1}$$

$$\frac{\mathrm{D}\rho}{\mathrm{D}t} = \frac{\partial \rho}{\partial t} + u_i \partial_i \rho = \frac{\partial \rho}{\partial t} + \partial_i (u_i \rho) - \rho \partial_i u_i. \tag{3.2}$$

Insertion into (2.4*c*) leads to

$$\bar{c}^2 \left(\frac{\partial \rho}{\partial t} + \partial_i (\rho u_i) \right) = \frac{\partial p}{\partial t} - \rho u_i \frac{\partial u_i}{\partial t} - \rho \left(u_i u_j - \bar{c}^2 \delta_{ij} \right) \partial_j u_i + \frac{1}{Re} \left(u_i \partial_j \tau_{ij} + G_0 \bar{G} \left(\tau_{ij} \partial_j u_i + \frac{1}{PrEc} \partial_k (k \, \partial_k \theta) \right) \right), \tag{3.3}$$

where δ_{ij} is Kronecker's delta. The left-hand side of (3.3) is the continuity equation; consequently, it follows that the right-hand side has to satisfy the solvability condition

$$\frac{\partial p}{\partial t} - \rho u_i \frac{\partial u_i}{\partial t} - \rho \left(u_i u_j - \bar{c}^2 \delta_{ij}\right) \partial_j u_i + \frac{1}{Re} \left(u_i \partial_j \tau_{ij} + G_0 \bar{G} \left(\tau_{ij} \partial_j u_i + \frac{1}{PrEc} \partial_k (k \partial_k \theta) \right) \right) = 0, \quad (3.4)$$

which for stationary flow reduces to the well-known gas dynamic equation

$$\left(u_i u_j - \bar{c}^2 \delta_{ij}\right) \partial_j u_i = 0 \quad (3.5)$$

in the limit $Re \to \infty$.

3.1.2. *Characterization of thermodynamic properties in channel core flow*

The behaviour of compressible flows as considered here strongly depends on the variation of the speed of sound – or, more precisely, the variation of the fundamental derivative Γ – with the thermodynamic state. It is, therefore, useful to identify regions in the p, $1/\rho$-diagram which exhibit significantly different properties in this respect. To this end, we adopt the single assumption that the fundamental derivative expressed in terms of ρ and s, i.e. $\Gamma = \Gamma(\rho, s)$, can be Taylor-expanded about the reference state characterized by the subscript 0:

$$\Gamma = \Gamma_0 + \Lambda_0(\rho - 1) + \tfrac{1}{2} N_0 (\rho - 1)^2 + \cdots, \quad (3.6)$$

introducing the quantities

$$\Lambda = (\partial \Gamma / \partial \rho)_s, \quad (3.7)$$

$$N = (\partial^2 \Gamma / \partial \rho^2)_s. \quad (3.8)$$

Contributions resulting from entropy changes are too small to influence the analysis to the order of accuracy considered here and therefore are not displayed in (3.6). As far as the magnitude of the Taylor coefficients Γ_0, Λ_0 and N_0 is concerned (which is of critical importance for the subsequent analysis), three different regimes in the p, $1/\rho$-diagram, and in the following, identified by the parameter n have to be distinguished. Undisturbed states located in regions $n = 2$ of figure 2(b) are characterized by $\Gamma \sim 1$ and consequently density variations are too small to lead to a sign change of the fundamental derivative. In that case, Γ can exhibit either positive or negative values. However, situations in which Γ can change its sign in the flow region of interest are possible for reference states which are located sufficiently close to the transition line $\Gamma = 0$. The region $n = 3$ in figure 2(b) is characterized by $\Gamma_0 \sim (\rho - 1)$, $\Lambda_0 \sim 1$, while region $n = 4$ (small neighbourhood of the point where an isentrope touches the transition line in figure 2b) is characterized by $\Gamma_0 \sim (\rho - 1)^2$, $\Lambda_0 \sim (\rho - 1)$, $N_0 \sim 1$. The case $n = 3$ identifies situations in which Γ changes sign only once during isentropic expansion, whereas Γ changes sign twice in the case $n = 4$.

3.2. *Formal asymptotic expansions and fundamental problem*

This section is a short summary of the corresponding section in Kluwick & Meyer (2010), included here for the sake of completeness. Deviations from Kluwick & Meyer (2010) result from the modified geometry of the problem and the alternative approach to the derivation of the upper-deck flow regime based on the solvability condition (3.4); however, since we implicitly require the nozzle geometry to be compatible with the triple-deck scaling found in the previous paper, in fact, all the former arguments carry over to the new problem. In the following, $(a)_b$ indicates that the flow quantity

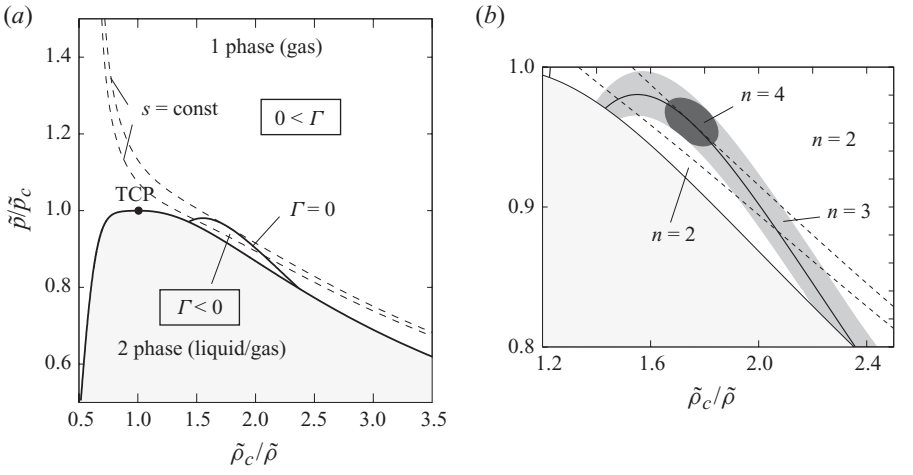

FIGURE 2. (*a*) Sketch of the pressure versus density diagram for a typical BZT fluid. The subscript c indicates thermodynamic quantities evaluated at the critical thermodynamical point TCP. (*b*) A close-up of the region of negative Γ and subdivision in regions with the asymptotic properties: $\Gamma \sim 1$, $\Gamma \gtrless 0$ $(n=2)$; $|\Gamma| \ll 1$, $(\partial\Gamma/\partial\rho)_s \sim 1$ $(n=3)$ and $|\Gamma| \ll 1$, $|(\partial\Gamma/\partial\rho)_s| \ll 1$, $(\partial^2\Gamma/\partial\rho^2)_s \sim 1$ $(n=4)$.

a is evaluated in the deck denoted by the subscript b, with b either l, m, u for lower-, main- or upper deck, respectively, and $0 < |\Delta a| \ll 1$ denotes a small perturbation of a. As outlined in § 3.1.2, the parameter $n \in \{2, 3, 4\}$ serves to characterize the thermodynamic regime of interest, cf. figure 2(*b*). The choice of n influences the scaling laws of the various decks.

Before starting with the discussion of formal asymptotic expansions, it is useful to recall the underlying physics of the triple-deck theory of strong interactions where boundary layer displacement no longer represents an effect of higher order as in the classical boundary layer theory but has to be accounted for at the same level of approximation as the behaviour of the outer inviscid flow.

As is well known, conservation of mass requires that the relative changes $\Delta F/F$ of the cross-sectional area F of stream tubes are of the same order of magnitude as the relative velocity changes $\Delta u/u$. Consequently, most of the displacement exerted by the interacting boundary layer is generated in a thin low-speed sublayer (lower deck) adjacent to the wall where the no-slip condition holds, cf. figure 3. Density changes in this region are negligible due to the smallness of the local Mach number and, therefore, the flow is governed by the incompressible form of the boundary layer equations. In the outer part of the boundary layer, the velocities are comparable in magnitude with those in the inviscid core and this (main deck) region thus simply acts to transfer the displacement resulting from velocity disturbances inside the lower deck essentially unchanged to the part of the core flow (upper deck), playing an active role in the interaction process where it causes an inviscid pressure response. The requirement that the flow in the upper-deck region is transonic and quasi-one-dimensional implies that its extent both in the streamwise and wall-normal directions is large compared with the boundary layer thickness. As a result, the pressure disturbances inside the main deck are independent of y, as in the classical boundary layer theory, thereby revealing its second important role as far as the interaction process is concerned: to

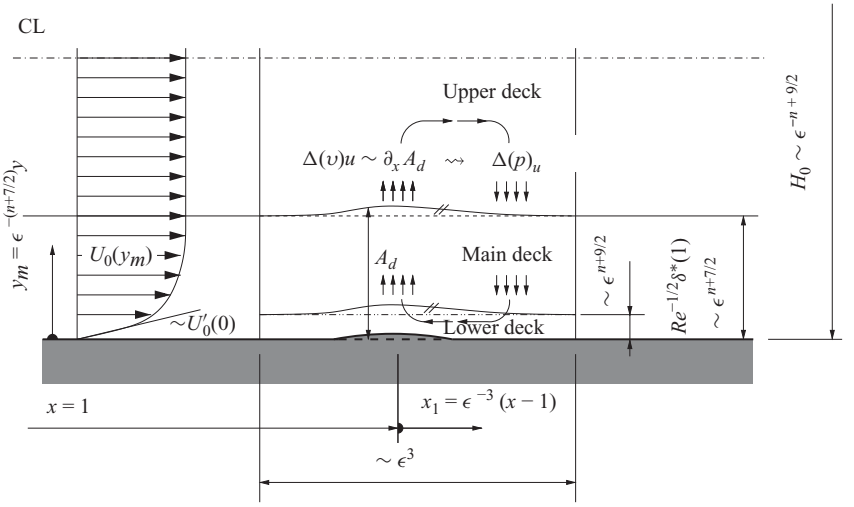

FIGURE 3. Triple-deck structure, scales of interaction region and sketch of the viscous–inviscid interaction mechanism. The displacement A_d generated in a thin sublayer of the upstream boundary layer, the lower deck, is transmitted unchanged to the upper deck by a passive main deck. There the induced vertical velocities $\Delta(v)_u$ evoke an inviscid pressure response $\Delta(p)_u$, which is transmitted unaltered back to the lower deck closing the 'interaction loop'. The small perturbation parameter ϵ is defined by (3.9).

transfer the pressure disturbances present at the base of the upper deck unchanged to the lower deck which, in fact, closes the 'interaction loop' included in figure 3.

Order-of-magnitude estimates based on the preceding physical considerations are summarized in table 2 of Kluwick & Meyer (2010) and uniquely determine the length scales of the various regions shown in figure 3 as well as the magnitudes of the perturbations of the field quantities therein. This has been outlined in detail in Kluwick & Meyer (2010) and, therefore, not repeated here, where we show that these scalings are consistent with deformations of the channel walls (originally taken to be flat) large enough to allow for a transition through the sonic state, i.e. large enough to act as the walls of a slender Laval nozzle.

We define the small perturbation parameter ϵ by

$$\epsilon = Re^{-1/(7+2n)}. \tag{3.9}$$

For the main deck, which comprises most of the interacting boundary layer, the analysis of Kluwick & Meyer (2010) suggests

$$x = 1 + \epsilon^3 x_1, \quad y = \epsilon^{n+7/2} y_m, \quad t = \epsilon^{5-2n} t_1, \tag{3.10}$$

where the subscript '1' denotes quantities used in all three decks, and

$$\left.\begin{aligned}
(u)_m &= U_0(y_m) + \epsilon u_m^{(1)}(x_1, y_m, t_1) + \cdots, \\
(v)_m &= \epsilon^{n+3/2} v_m^{(1)}(x_1, y_m, t_1) + \cdots, \\
(\rho)_m &= R_0(y_m) + \epsilon \rho_m^{(1)}(x_1, y_m, t_1) + \cdots, \\
(p)_m &= p_0 + \epsilon^2 p_1^{(1)}(x_1, y_m, t_1) + \cdots.
\end{aligned}\right\} \tag{3.11}$$

Here, $U_0(y_m)$ and $R_0(y_m)$ represent the velocity and density profiles, respectively, in the undisturbed boundary layer at $x = 1$ with $U_0 = R_0 = 1$ for $y_m \to \infty$ at the edge of the boundary layer, see figure 3. Substitution of (3.11) and (3.10) into the full

Navier–Stokes equations (2.4*a*)–(2.4*c*) and taking the limit $Re \to \infty$ yields that the leading-order perturbations of the velocity components and density are unaffected by pressure and viscous forces and can be expressed in terms of a (so far unknown) displacement function $-A_1(x_1, t_1)$:

$$u_m^{(1)} = A_1 U_0', \quad v_m^{(1)} = -\partial_{x_1} A_1 U_0, \quad \rho_m^{(1)} = A_1 R_0'. \tag{3.12}$$

The main-deck problem does not depend explicitly on the time to the leading order under the applied time scaling (3.10). The pressure disturbances

$$p_1^{(1)} = p_1^{(1)}(x_1, t_1) \tag{3.13}$$

are enforced by the induced pressure disturbances in the upper deck and, therefore, do not depend on the lateral distance y_m. As pointed out before, the main deck behaves passively and primarily acts to transfer the pressure disturbances generated in the upper-deck flow unchanged to the lower deck and the displacement effects exerted by the lower-deck reaction to the pressure disturbances unchanged back to the upper deck. The displacement effect evoked by the interacting boundary layer, which can be observed by evaluating equation (3.12) at the edge of the boundary layer,

$$u_m^{(1)} = \rho_m^{(1)} = 0, \quad v_m^{(1)} = -\partial_{x_1} A_1, \quad y_m \to \infty, \tag{3.14}$$

leads to a reduction $A_d = \epsilon^{n+7/2}\delta^*(1) - \epsilon^{n+9/2} A_1(x_1, t_1)$ of the effective area of cross-section for the upper-deck flow, cf. figure 3,

$$(H)_u = \epsilon^{-n+9/2} H_{01} - 2(\epsilon^{n+7/2}\delta^*(1) - \epsilon^{n+9/2} A_1(x_1, t_1) + \cdots). \tag{3.15}$$

Here, the first term within the brackets accounts for the contribution of the oncoming unperturbed boundary layer. The value $\delta^*(1)$ at $x = 1$ (defining the location of the interaction region) depends on the upstream history of the flow but does not affect the essential properties of the interaction process. The vertical coordinate

$$(y)_u = \epsilon^{-n+9/2} y_u \tag{3.16}$$

in the upper deck has to scale in the same way as the height H_0 of the channel. For the other relevant flow quantities of the upper-deck flow, we write

$$\left.\begin{aligned} (u)_u &= 1 + \epsilon^2 u_u^{(1)}(x_1, y_u, t_1) + \cdots, \\ (v)_u &= \epsilon^{n+3/2} v_u^{(1)}(x_1, y_u, t_1) + \cdots, \\ (\rho)_u &= 1 + \epsilon^2 \rho_u^{(1)}(x_1, y_u, t_1) + \cdots, \\ (c)_u &= 1 + \epsilon^2 c_u^{(1)}(x_1, y_u, t_1) + \cdots, \\ (p)_u &= p_0 + \epsilon^2 p_u^{(1)}(x_1, y_u, t_1) + \cdots \end{aligned}\right\} \tag{3.17}$$

and

$$1 - M_0^2 = \epsilon^{2(n-1)} K, \tag{3.18}$$

$$\Gamma_0 = \epsilon^{2(n-2)} \bar{\Gamma}, \quad \Lambda_0 = \epsilon^{max\{2(n-3),0\}} \bar{\Lambda}, \quad N_0 = \bar{N}. \tag{3.19}$$

Here $K = O(1)$ denotes a scaled transonic similarity parameter; for $K > 0$ the oncoming undisturbed core-region flow is subsonic and for $K < 0$ supersonic. Furthermore, the material-dependent parameters $\bar{\Gamma}$, $\bar{\Lambda}$, $\bar{N}$ defined in (3.19) are $O(1)$.

From (2.4*a*) and (2.4*b*) after integration with respect to x_1, one then finds to leading order that $u_u^{(1)}$, $\rho_u^{(1)}$ and $p_u^{(1)}$ do not depend on y_u and have to satisfy the relationships

$$u_u^{(1)}(x_1, t_1) = -\rho_u^{(1)}(x_1, t_1) = -p_u^{(1)}(x_1, t_1), \tag{3.20}$$

also known from other studies of transonic flows and expressing the fact that a sonic state corresponds to an extremum (maximum in the case of regular, perfect-gas-like fluids) of the mass-flux versus Mach number diagram. Matching with the main-deck flow (3.14) reveals that the pressure in the upper deck is, to the leading order, the same as in the main deck (and in the lower deck as well):

$$p_u^{(1)}(x_1, t_1) = p_1^{(1)}(x_1, t_1). \tag{3.21}$$

As shown in § 3.1.1, the pressure, density and velocity components in the upper deck have to satisfy the solvability condition (3.4), its asymptotic representation being

$$\frac{\partial p_1^{(1)}}{\partial t_1} + \frac{1}{2}\frac{\partial}{\partial x_1} J_{[n]}\big(p_1^{(1)}; K, \bar{\Gamma}, \bar{\Lambda}, \bar{N}\big) = -\frac{1}{2}\left(\frac{\partial v}{\partial y}\right)_u + \cdots. \tag{3.22}$$

Here we have used relation (3.20) and, from Kluwick & Meyer (2010), the expansion

$$\begin{aligned}(u - \bar{c}) = M_0 - 1 - \Gamma_0(\rho - 1) + \tfrac{1}{2}\big(\Gamma_0^2 - \Gamma_0 - \Lambda_0\big)(\rho - 1)^2 \\ + \tfrac{1}{6}\big(3\Gamma_0^3 - 3\Gamma_0^2 + 14\Gamma_0 - 4\Lambda_0 + 5\Gamma_0\Lambda_0 - N_0\big)(\rho - 1)^3 + \cdots.\end{aligned} \tag{3.23}$$

As in Kluwick & Meyer (2010), the perturbation of the mass flux density is defined as

$$J_{[n]}(p; K, \bar{\Gamma}, \bar{\Lambda}, \bar{N}) := \begin{cases} -Kp - \bar{\Gamma}p^2, & n = 2, \\ -Kp - \bar{\Gamma}p^2 - \frac{1}{3}\bar{\Lambda}p^3, & n = 3, \\ -Kp - \bar{\Gamma}p^2 - \frac{1}{3}\bar{\Lambda}p^3 - \frac{1}{12}\bar{N}p^4, & n = 4. \end{cases} \tag{3.24}$$

Since the upper-deck flow is one-dimensional to leading order, the continuity equation has to satisfy

$$\left(\frac{\partial}{\partial t}(\rho H) + \partial_x(\rho u H)\right)_u = 0 + \cdots \tag{3.25}$$

at this level of approximation, which after some manipulations yields

$$\left(\frac{\partial}{\partial t}\rho + \partial_x(\rho u) + \rho u\frac{\partial_x H}{H}\right)_u = -\left(\rho\frac{1}{H}\frac{\partial}{\partial t}H\right)_u + \cdots. \tag{3.26}$$

A comparison with the two-dimensional form of the continuity equation (2.4*a*),

$$\frac{\partial}{\partial t}\rho + \partial_x(\rho u) + \partial_y(\rho v) = 0, \tag{3.27}$$

and taking into account the asymptotic expansions (3.17) and (3.15) and the scalings t and x according to (3.10) suggests the dependence of the local boundary-layer displacement perturbation on the induced vertical upper-deck velocity perturbations:

$$\left(\frac{\partial v}{\partial y}\right)_u = \epsilon^{2n-3}\frac{2}{H_{01}}\partial_{x_1}A_1 + \cdots. \tag{3.28}$$

The requirement of quasi-one-dimensional flow in the core region forces the v-component there to vanish in leading order. Evaluation of the continuity equation then implies that the next higher correction must vary linearly with distance from the channel axis. As a consequence, $(\partial v/\partial y)_u$ is proportional to v_u at the channel wall so that (3.28) is seen to represent the proper generalization of a relationship between v and the streamwise variation of the displacement thickness known from the classical

boundary layer theory to the case of strong interactions. The solvability condition then takes on the final form

$$\frac{\partial p_1^{(1)}}{\partial t_1} + \frac{1}{2}\frac{\partial}{\partial x_1} J_{[n]}\big(p_1^{(1)}; K, \bar{\Gamma}, \bar{\Lambda}, \bar{N}\big) = -\frac{1}{H_{01}}\frac{\partial A_1}{\partial x_1}, \tag{3.29}$$

relating the induced pressure disturbances inside the upper deck and the displacement function accounting for the boundary-layer flow response. It is worthwhile to note that in Kluwick & Meyer (2010) the interaction law (3.29) has been obtained from the compatibility relations along left-running characteristics employing physical arguments. Here, (3.29) is obtained from a mathematical solvability condition, which has been shown to be related to the gasdynamic equation for inviscid flow in § 3.1.1. Because of this connection, (3.29) can be interpreted as a version of the continuity equation, which is the reason for originally introducing $J_{[n]}$ as the leading-order perturbation of the upper-deck mass flux density. Indeed, as shown heuristically by Kluwick (2009), the qualitative form of the interaction equation for steady flows can be inferred directly from a mass balance which has the advantage that it applies equally well to the different and at first sight unrelated problem of weak hydraulic jumps (Kluwick *et al.* 2010).

The displacement function $-A_1(x_1, t_1)$ is an outcome of the solution to the lower-deck problem which is obtained by introducing the following expansions (given here in a form which eliminates most of the parameters characterizing the unperturbed flow in the resulting distinguished limit):

$$\left.\begin{aligned}
(u)_l &= \epsilon R_0(0)^{-1/2}|2\bar{\Gamma}/K|^{-1/2}U(X, Y, T) + \cdots,\\
(v)_l &= \epsilon^{n+5/2}\mu_w R_0(0)^{-1/2}U_0'(0)|2\bar{\Gamma}/K|^{1/2}\,(V(X, Y, T) + U\ \partial S(X)/\partial X) + \cdots,\\
(\rho)_l &= R_0(0) + \cdots,\\
(p)_l &= p_0 + \epsilon^2|2\bar{\Gamma}/K|^{-1}P(X, T) + \cdots,
\end{aligned}\right\} \tag{3.30}$$

where

$$(y)_l = \epsilon^{n+9/2}R_0(0)^{-1/2}U_0'(0)^{-1}|2\bar{\Gamma}/K|^{-1/2}(Y + S(X)) \tag{3.31}$$

and

$$x_1 = \mu_w^{-1}R_0(0)^{-1/2}U_0'(0)^{-2}|2\bar{\Gamma}/K|^{-3/2}X, \tag{3.32}$$

$$t_1 = \mu_w^{-1}R_0(0)^{-1/2}U_0'(0)^{-2}|\bar{\Gamma}|^{-1}|2\bar{\Gamma}/K|^{-1/2}T, \tag{3.33}$$

$$A_1 = R_0(0)^{-1/2}U_0'(0)^{-1}|2\bar{\Gamma}/K|^{-1/2}(A(X, T) - S(X)). \tag{3.34}$$

Here, $S(X)$ denotes the scaled variation of the channel area of cross-section

$$s_{\mathscr{N}}(x) = \epsilon^{n+9/2}R_0(0)^{-1/2}U_0'(0)^{-1}|2\bar{\Gamma}/K|^{-1/2}S(X), \tag{3.35}$$

with $\lim_{X\to\infty} S(X) := S_\infty$ satisfying the downstream condition

$$-\delta H_0 = \epsilon^{n+9/2}R_0(0)^{-1/2}U_0'(0)^{-1}|2\bar{\Gamma}/K|^{-1/2}S_\infty. \tag{3.36}$$

Here $U_0'(0)$, $R_0(0)$ and μ_w are, respectively, the slope of the horizontal velocity flow field, the density and the dynamic viscosity in the oncoming undisturbed boundary layer at $x = 1$ (cf. figure 3) evaluated at the channel wall. Insertion into the full Navier–Stokes equation yields the fundamental lower-deck equations in canonical, i.e.

parameter-free, form as

$$\frac{\partial U}{\partial X}+\frac{\partial V}{\partial Y}=0, \tag{3.37}$$

$$U\frac{\partial U}{\partial X}+V\frac{\partial U}{\partial Y}=-\frac{\partial P}{\partial X}+\frac{\partial^2 U}{\partial Y^2}, \tag{3.38}$$

supplemented by the no-slip condition at the wall

$$U=V=0, \quad Y=0, \tag{3.39}$$

the conditions of matching with the undisturbed non-interacting oncoming boundary layer

$$U=Y, \quad V=0, \quad P=0, \quad X\to-\infty, \tag{3.40}$$

and the conditions of matching with the main-deck flow

$$U=Y+A(X,T), \quad Y\to\infty. \tag{3.41}$$

Because of the special functional form of (3.30)–(3.34), also known as Prandtl's transposition theorem (Prandtl 1938), the transformed lower-deck problem (3.37)–(3.41) becomes independent of the contour of the surface-mounted hump $S(X)$, and the no-slip condition is prescribed at an undisturbed plane wall. To this end, the boundary layer displacement exerted on the upper deck, $-A_1$, is split into a purely viscous part, $-A$, and a purely geometrical part, S, cf. (3.34). The interaction relation (3.29), which closes the quasi-steady lower-deck problem (3.37)–(3.41), then takes on the canonical form

$$-\frac{\partial P}{\partial T}+\frac{\partial}{\partial X}\,G_{[n]}\left(P;K,\Gamma_{-\infty},\Lambda_{-\infty},N_{-\infty}\right)=Q\frac{\partial}{\partial X}\left(A-S\right), \tag{3.42}$$

where $G_{[n]}$ is a scaled version of $-J_{[n]}$ defined by

$$G_{[n]}(P;K,\Gamma,\Lambda,N):=\begin{cases}\operatorname{sign}(K)P+\frac{1}{2}\Gamma P^2, & n=2,\\ \operatorname{sign}(K)P+\frac{1}{2}\Gamma P^2+\frac{1}{6}\Lambda P^3, & n=3,\\ \operatorname{sign}(K)P+\frac{1}{2}\Gamma P^2+\frac{1}{6}\Lambda P^3+\frac{1}{24}N P^4, & n=4.\end{cases} \tag{3.43}$$

The remaining parameters in the canonical formulation are defined as

$$\Gamma_{-\infty}=\bar{\Gamma}\left|\bar{\Gamma}\right|^{-1}, \tag{3.44}$$

$$\Lambda_{-\infty}=\bar{\Lambda}|2\bar{\Gamma}/K|^{-1}\left|\bar{\Gamma}\right|^{-1}, \tag{3.45}$$

$$N_{-\infty}=\bar{N}|2\bar{\Gamma}/K|^{-2}\left|\bar{\Gamma}\right|^{-1}, \tag{3.46}$$

$$Q=2^{-1}R_0(0)^{-1/2}U_0'(0)^{-1}|2\bar{\Gamma}/K|^{3/2}\left|\bar{\Gamma}\right|^{-1}H_{01}^{-1}>0, \tag{3.47}$$

and represent similarity parameters insofar as they account for both material and fluid mechanic properties of the oncoming flow. The subscript $-\infty$ indicates that the material parameters are evaluated immediately upstream of the interaction region ($X\to-\infty$). Integration of the interaction law (3.42) for steady flows (which is the focus of the present paper) with respect to X gives

$$G_{[n]}(P)-Q\left(A-S\right)=j_1^{(1)}=0, \tag{3.48}$$

where the dependence of $G_{[n]}$ on the parameters has been suppressed. Since for $X\to-\infty$ $(P,A,S)\to(0,0,0)$, the integration constant $j_1^{(1)}$ has to be zero.

The leading order of the Mach number variation in the interacting channel core follows from the relation (cf. Kluwick & Meyer 2010)

$$(M-1)/\epsilon^{2(n-1)} = -4^{-1}|K|^2|\bar{\Gamma}|^{-1}\mathrm{d}G_{[n]}/\mathrm{d}P + \cdots . \tag{3.49}$$

From (3.49), it is evident that the Mach number varies non-monotonically in the case of dense gases exhibiting mixed nonlinearity, i.e. $n=3$ and $n=4$.

In the following, we give a brief summary of important properties of the solution to the interaction problem (3.37)–(3.48) outlined in Kluwick & Meyer (2010), which is relevant for the discussion of specific numerical solutions in § 4.

3.3. *Some properties of general solutions to the interaction problem*

In Kluwick & Meyer (2010), the far downstream ($X \to -\infty$) and upstream behaviours ($X \to \infty$) of the existing non-trivial eigensolutions to the interaction problem for a constant area of cross-section have been discussed in detail. However, the results of the asymptotic analysis apply equally well to the description of the far upstream and downstream behaviours of an arbitrary solution to the general problem under the weaker condition that the variation of the wall contour only vanishes upstream and downstream of the nozzle $S(X)$, i.e.

$$\frac{\partial S}{\partial X} = 0, \quad |X| > C, \tag{3.50}$$

for some given constant $0 < C < \infty$.

Given a nozzle satisfying condition (3.50), it then follows:

(i) If the oncoming flow is supersonic, an upstream influence of the nozzle on the flow can be observed, i.e. a free-interacting part of the solution, which extends into regions of a constant channel crossflow section and is linked to the existence of non-trivial eigensolutions. In this connection, it is interesting to note that perturbations cannot propagate upstream in supersonic flows but they can in the subsonic portion of the boundary layer which gives rise to the *Oswatitsch–Wieghardt mechanism*, cf. Lighthill (2000) or Stewartson (1981): 'The underlying physical argument of this phenomenon has been given earlier by Oswatitsch & Wieghardt (1946) – in supersonic flow any change in pressure produces changes in the displacement thickness of the boundary layer which tend to reinforce the original change'. The asymptotic form of the free-interaction part far upstream of the nozzle is expressed by exactly the same expansions given in Kluwick & Meyer (2010). Since the objective of this paper is to discuss the conversion of subsonic flow to the supersonic flow regime, the associated properties of supersonic oncoming flows will not be treated here in more detail.

(ii) However, if the oncoming core-region flow is subsonic, 'the Oswatitsch–Wieghardt argument is reversed and the disturbance to the basic flow must die away' (Stewartson 1981). Consequently, there exist no non-trivial eigensolutions and deviations from undisturbed flow states are triggered within the nozzle part and the resulting flow field evolves downstream. Upstream of the nozzle, no influence of its presence can be felt.

(iii) Far downstream of the nozzle, the interacting boundary layer flow approaches the undisturbed boundary layer flow again in a weak algebraic manner, i.e.

$$A(X) \sim A^{(1)}X^{-1/3} + \cdots , \quad C < X \to \infty, \tag{3.51}$$

where $A^{(1)}$ denotes a problem-dependent constant.

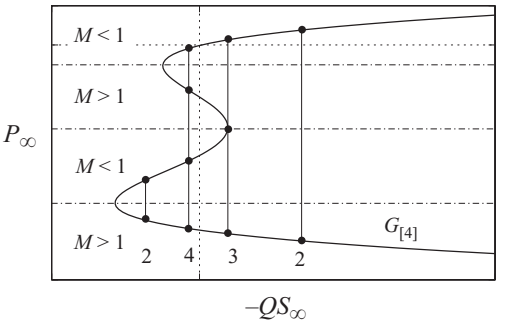

FIGURE 4. Downstream pressure P_∞ in dependence of the variation of the downstream channel area of cross-section proportional to $-S_\infty$ for the example of a fourth-order mass flux density $G_{[4]}$.

(iv) Consequently, because of (3.48) taking into account $(S, A) \to (S_\infty, 0)$ for $X \to \infty$, the far downstream flow state in the upper deck has to satisfy the relation

$$G_{[n]}(P_\infty) = -QS_\infty, \tag{3.52}$$

which gives n-possible solutions for the downstream value P_∞, in general. Which far downstream state is realized depends, as discussed in § 4.2, on the geometrical properties of the nozzle. Again, the downstream state of P is reached in a weak algebraic manner, e.g. if $\partial G_{[n]}(P)/\partial P := G'_{[n]}(P) \neq 0$,

$$P(X) \sim P_\infty + \frac{QP^{(1)}}{G'_{[n]}(P_\infty)} X^{-1/3} + \cdots, \quad C < X \to \infty, \tag{3.53}$$

where $P^{(1)}$ denotes a problem-dependent constant.

3.4. *The far-downstream state in slender nozzles*

An important, if not the most important, parameter in the Laval nozzle operation is the pressure level, or, in other words, the Mach number (cf. (3.49)) attainable far downstream of the nozzle, that is, in the present case downstream of the interaction region for $X \to \infty$. As is evident by relation (3.52), the downstream pressure P_∞ depends only on the value of the parameter Q governing the intensity of the interaction process and the (scaled) variation of the area of cross-section at nozzle exit with respect to the area of cross-section at nozzle entry given by $-2S_\infty$ (cf. (3.35) and figure 1), provided that $S \equiv S_\infty$ for $X > C > 0$. Since $G_{[n]}$ is a polynomial of order n (cf. (3.43)), the accessible downstream state P_∞ is not unique (cf. (3.52)), and each value of P_∞ corresponds to a different Mach number regime in the core region far downstream of the interaction region (cf. (3.49)). Considering the example shown in figure 4 illustrating the situation for a mass-flux density perturbation $-G_{[n]}$ of fourth order, two, three or even four downstream states are possible for a given value of QS_∞, as indicated by the vertical lines labelled 2, 3 and 4, respectively, in figure 4. (Note that $M - 1$ is proportional to the slope of $-G_{[n]}$, cf. (3.49) and, consequently, the three extrema of $G_{[4]}$ in figure 4 correspond to three sonic states, i.e. $M_\infty = 1$.)

In the following discussion of the various resulting flow patterns in slender Laval nozzles obtained by numerical solutions presented in §§ 4.2.1 and 4.2.2, we assume that $S \equiv S_\infty = 0$ for $X > C > 0$. As far as the discussion of the observed flow phenomena is concerned, this assumption does not mean a loss of generality. In § 4.3, we briefly comment on the more general case $S \to S_\infty$ for $X \to \infty$.

4. Numerical results

4.1. *Numerical method*

The fundamental lower-deck problem equations (3.37)–(3.41) and the interaction law (3.42) for steady flows with $\partial P/\partial T \equiv 0$ in § 3.2 are discretized by means of finite differences of second order. In Kluwick & Meyer (2010), we adopted a marching or shooting technique in order to obtain numerical solutions integrating the equations downstream in the main-flow direction starting from a known initial flow profile far upstream. For conventional boundary layer equations, where the pressure is imposed by the known outer solution, the well-posedness of such a marching technique is guaranteed by the parabolic character of the equations. For triple-deck problems involving a local interaction relationship, the well-posedness requires that $U > 0$ in the lower-deck flow field throughout, i.e. the boundary layer flow remains attached. Consequently, special precautions have to be taken, like the usage of the FLARE approximation (Reyhner & Flügge 1968), when dealing with separated flow regions in a marching approach. In contrast, here we aim to solve the full set of algebraic equations obtained by the finite-difference representation of the governing equations on a computational grid comprising the whole physical domain in one single computational step, thus bypassing the issue of stability of the marching technique. In addition, parameter variations can now be achieved in a very efficient way, making up for the increased main-memory consumption, cf. § 4.1.1.

To this end, the physical domain $(X, Y) \in \mathbb{R} \times \mathbb{R}^+$ is mapped onto the bounded computational domain $(\xi, \eta) \in [-1, 1] \times [0, 1/\alpha_s]$. The mapping $\xi \mapsto X(\xi) \in C^1([-1, 1])$ is sought in the form

$$X(\xi) = \begin{cases} X_u(\xi), & -1 \leqslant \xi < \Xi_u, \\ X_m(\xi), & \Xi_u \leqslant \xi \leqslant \Xi_d, \\ X_d(\xi), & \Xi_d < \xi \leqslant 1, \end{cases} \tag{4.1}$$

introducing three functions X_u, X_d and X_m:

$$X_u(\xi) = X_{su} + \frac{X_{sd} - X_{su}}{\Xi_d - \Xi_u} \frac{1 + \Xi_u}{2m_u} \left(\frac{1}{\left(1 - \dfrac{\xi - \Xi_u}{1 + \Xi_u}\right)^{m_u}} - \frac{1}{\left(1 + \dfrac{\xi + \Xi_u}{1 + \Xi_u}\right)^{m_u}} \right), \tag{4.2}$$

$$X_m(\xi) = X_{su} + \frac{X_{sd} - X_{su}}{\Xi_d - \Xi_u}(\xi - \Xi_u), \tag{4.3}$$

$$X_d(\xi) = X_{sd} + \frac{X_{sd} - X_{su}}{\Xi_d - \Xi_u} \frac{1 - \Xi_d}{2m_d} \left(\frac{1}{\left(1 - \dfrac{\xi - \Xi_d}{1 - \Xi_d}\right)^{m_d}} - \frac{1}{\left(1 + \dfrac{\xi + \Xi_d}{1 - \Xi_d}\right)^{m_d}} \right). \tag{4.4}$$

The parameters m_u and m_d control the grid spacing in the X-direction far upstream and downstream of the nozzle. Most importantly, X_m is a linear mapping of an interior region $[X_{su}, X_{sd}]$ of the physical domain onto an interior region $[\Xi_u, \Xi_d]$ of the computational domain. The complicated form of X_u and X_d is a consequence of the requirement $X(\xi) \in C^1([-1, 1])$, which is accounted for by the conditions $X_u'(\Xi_u-) = X_m'(\Xi_u+)$ and $X_m'(\Xi_d-) = X_u'(\Xi_d+)$. Here, the prime denotes the derivative

with respect to ξ. With the map $\eta \mapsto Y(\eta) \in C^2([0, 1/\alpha_s])$ in the form of

$$Y(\eta) = Y_s \left(\frac{1}{1-\alpha_s \eta} - \frac{1}{1+\alpha_s \eta} \right), \tag{4.5}$$

introducing the scaling parameters Y_s and α_s, the representation of the uniform numerical grid in the new coordinates (ξ, η) is given by

$$(\xi_i, \eta_j) = (-1 + i\Delta\xi, j\Delta\eta), \quad i = 0, \ldots, N_i, \quad j = 0, \ldots, N_j - 1. \tag{4.6}$$

The uniform grid spacings in the ξ-direction and the η-direction are given by $\Delta\xi = 2/N_i$ and $\Delta\eta = 1/N_j$, respectively, where N_i denotes the number of grid points in the X-direction and N_j denotes the number of grid points in the Y-direction.

For the numerical treatment of the fundamental lower-deck problem, the transformation $\bar{U} = U - Y$ is introduced and V in the momentum equation (3.38) is expressed by means of the continuity equation (3.37):

$$V = -\int_0^Y \frac{\partial \bar{U}}{\partial X}(X, \bar{Y}) \mathrm{d}\bar{Y} = -\int_0^\eta \frac{1}{X'(\xi)} \frac{\partial \bar{U}}{\partial \xi}(\xi, \bar{\eta}) Y'(\bar{\eta}) \mathrm{d}\bar{\eta}. \tag{4.7}$$

The momentum equation then can be cast into the following form:

$$(Y + \bar{U})\xi' \frac{\partial \bar{U}}{\partial \xi} - \left(1 + \eta' \frac{\partial \bar{U}}{\partial \eta}\right) \int_0^\eta \xi' \frac{\partial \bar{U}}{\partial \xi} Y' \mathrm{d}\bar{\eta} = -\xi' \frac{\partial P}{\partial \xi} + \eta'' \frac{\partial \bar{U}}{\partial \eta} + \eta' \frac{\partial^2 \bar{U}}{\partial \eta^2}, \tag{4.8}$$

where we make use of the correlation between the derivative of a function and its inverse

$$\xi'(X) = 1/X'(\xi), \quad \eta'(Y) = 1/Y'(\eta), \quad \eta''(Y) = -Y''(\eta)/Y'(\eta)^3. \tag{4.9}$$

All field quantities are computed at the grid points; we write $(\cdot)_{i,j}$ for a field quantity at the grid point (ξ_i, η_j) and $(\cdot)_{i-1/2,j}$ for an interpolated value at the intermediate point

$$(\xi_{i-1/2}, \eta_j) = (-1 + (i - 1/2)\Delta\xi, j\Delta\eta), \quad i = 1, \ldots, N_i, \quad j = 0, \ldots, N_j - 1. \tag{4.10}$$

As mentioned earlier, the momentum equation in the form (4.8) is discretized by means of finite differences of second-order accuracy. Specifically, different versions, one for regions with and one for regions without flow separation, are used. In the attached flow regions characterized by $U_{i,j} = Y_{i,j} + \bar{U}_{i,j} > 0$, (4.8) is approximated at the intermediate grid points $(\xi_{i-1/2}, \eta_j)$, whereas in regions of separated flow (4.8) is approximated at the grid points (ξ_i, η_j); cf. table 2 for details of the finite-difference formulae. The integral in (4.7) is evaluated according to the trapezoidal rule. Numerical experiments showed that the discretization based solely on the first type of discretization is superior to a discretization based on backward differences in regions without flow separation, also in the light of a reduced computational main-memory consumption. However, we also found that it is not always satisfactory in larger regions of flow separation as indicated by a significantly jagged wall shear-stress distribution close to the reattachment point, which are successfully suppressed by the combined scheme. Finally, we noted that the condition number of the whole algebraic system of equations becomes very poor in such cases apparently leading to numerical errors which are not small in comparison to the relatively small $\bar{U}$-values in separation regions. The idea behind the different type of discretization in regions with flow separation is to use information at three neighbouring grid points instead of only two in order to compute the derivatives in the ξ-direction. The combined scheme did

$U_{i,j} > 0$

Expression	Finite-difference representation of second order
$\left(\dfrac{\partial(\cdot)}{\partial\xi}\right)_{i-\frac{1}{2},j}$	$\left(\dfrac{(\cdot)_{i,j}-(\cdot)_{i-1,j}}{\Delta\xi}\right)$
$\left(\dfrac{\partial\bar{U}}{\partial\eta}\right)_{i-\frac{1}{2},j}$	$\dfrac{1}{2}\left(\dfrac{\bar{U}_{i,j+1}-\bar{U}_{i,j-1}}{2\Delta\eta}+\dfrac{\bar{U}_{i-1,j+1}-\bar{U}_{i-1,j-1}}{2\Delta\eta}\right)$
$\left(\dfrac{\partial^2\bar{U}}{\partial\eta^2}\right)_{i-\frac{1}{2},j}$	$\dfrac{1}{2}\left(\dfrac{\bar{U}_{i,j+1}-2\bar{U}_{i,j}+\bar{U}_{i,j-1}}{\Delta\eta^2}+\dfrac{\bar{U}_{i-1,j+1}-2\bar{U}_{i-1,j}+\bar{U}_{i-1,j-1}}{\Delta\eta^2}\right)$
$V_{i-\frac{1}{2},j}$	$-\dfrac{1}{X'(\xi_{i-1/2})}\displaystyle\sum_{k=1}^{j}\dfrac{1}{2}\left\{\left(\dfrac{\partial\bar{U}}{\partial\xi}\right)_{i-\frac{1}{2},k}+\left(\dfrac{\partial\bar{U}}{\partial\xi}\right)_{i-\frac{1}{2},k-1}\right\}\{Y(\eta_k)-Y(\eta_{k-1})\}$

$U_{i,j} < 0$

Expression	Finite-difference representation of second order
$\left(\dfrac{\partial(\cdot)}{\partial\xi}\right)_{i,j}$	$\left(\dfrac{3(\cdot)_{i,j}-4(\cdot)_{i-1,j}+(\cdot)_{i-2,j}}{2\Delta\xi}\right)$
$\left(\dfrac{\partial\bar{U}}{\partial\eta}\right)_{i,j}$	$\left(\dfrac{\bar{U}_{i,j+1}-\bar{U}_{i,j-1}}{2\Delta\eta}\right)$
$\left(\dfrac{\partial^2\bar{U}}{\partial\eta^2}\right)_{i,j}$	$\left(\dfrac{\bar{U}_{i,j+1}-2\bar{U}_{i,j}+\bar{U}_{i,j-1}}{\Delta\eta^2}\right)$
$V_{i,j}$	$-\dfrac{1}{X'(\xi_i)}\displaystyle\sum_{k=1}^{j}\dfrac{1}{2}\left\{\left(\dfrac{\partial\bar{U}}{\partial\xi}\right)_{i,k}+\left(\dfrac{\partial\bar{U}}{\partial\xi}\right)_{i,k-1}\right\}\{Y(\eta_k)-Y(\eta_{k-1})\}$

TABLE 2. Different formulae used in the numerical scheme. Here, $U_{i,j} > 0$ denotes attached flow regions and $U_{i,j} < 0$ denotes separated flow regions.

seem to lead to the best results in the end. Note that an initial strategy of a problem formulation on the basis of the streamfunction has been abandoned in favour of the described procedure because of the numerical problems in regions of flow separation.

The matching condition (3.41) is implemented as $A = \bar{U}(X, Y_{max} = Y(1))$. This is justified because of the exponential decay of $\bar{U}$ for $Y \gg 1$ (cf. Kluwick & Meyer 2010). The no-slip condition at the wall requires $\bar{U}_{i,0} = 0$, for $i = 0, \ldots, N_i$, and matching with the undisturbed boundary layer upstream results in the conditions $\bar{U}_{0,j} = 0$, for $j = 0, \ldots, N_j - 1$.

The interaction law for the steady upper-deck flow (3.42),

$$\frac{\mathrm{d}}{\mathrm{d}X}\big(G_{[n]}(P) - Q(A-S)\big) = \frac{1}{X'(\xi)}\frac{\mathrm{d}}{\mathrm{d}\xi}\big(G_{[n]}(P) - Q(A-S)\big) = 0, \tag{4.11}$$

is approximated by $\mathscr{G}_i = 0 \quad \forall i$, where $\mathscr{G}_i$ is defined by

$$\mathscr{G}_i := \begin{cases} \dfrac{1}{X'_i}\dfrac{\big(G_{[n]}(P_{i+1}) - Q(A_{i+1}-S_{i+1})\big) - \big(G_{[n]}(P_{i-1}) - Q(A_{i-1}-S_{i-1})\big)}{2\Delta\xi}, \\ \qquad\qquad\qquad\qquad\qquad\qquad i = 1, \ldots, N_i - 1, \\ \dfrac{1}{X'_{i-1/2}}\dfrac{\big(G_{[n]}(P_i) - Q(A_i-S_i)\big) - \big(G_{[n]}(P_{i-1}) - Q(A_{i-1}-S_{i-1})\big)}{\Delta\xi}, \\ \qquad\qquad\qquad\qquad\qquad\qquad i = N_i, \end{cases} \tag{4.12}$$

Section	N_i	N_j	Ξ_u	Ξ_d	m_u	m_d	X_{su}	X_{sd}	Y_s	α_s	
4.2.1	800	50	$100/N_i$	$500/N_i$	1.3	1.3	0	3	0.2	0.98	
4.2.2	800	50	$100/N_i$	$500/N_i$	1.3	1.3	0	35	0.2	0.98	($L_{\mathcal{N}}=10$)
4.2.2	800	50	$100/N_i$	$500/N_i$	1.3	1.3	−10	25	0.2	0.98	($L_{\mathcal{N}}=15$)
4.3	1400	100	$300/N_i$	$1100/N_i$	1.3	1.3	−6	6	0.2	0.98	

TABLE 3. Various parameter values used in the numerical computations discussed in §§ 4.2 and 4.3; $L_{\mathcal{N}}$ is defined in § 4.2.

and $X'_{i-1/2}=X'(-1+(i-1/2)\Delta\xi)$. Equation (4.12) is a finite-difference approximation to (4.11) of second order at the point (ξ_i).

The resulting system of $d=N_i\ (N_j+1)$ algebraic nonlinear equations

$$\boldsymbol{F}(\boldsymbol{s})=\boldsymbol{0},\quad \boldsymbol{F},\boldsymbol{s}\in\mathbb{R}^d, \tag{4.13}$$

with $\boldsymbol{s}$ being the d-dimensional solution vector is solved by a variant of Powell's hybrid algorithm (e.g. Powell 1970). The sparsity of the Jacobian $D_{\boldsymbol{s}}\boldsymbol{F}$ of $\boldsymbol{F}$ is exploited by the implementation of the sparse solver routine PARDISO (Schenk, Gärtner & Fichtner 2000; Schenk & Gärtner 2004; Schenk & Gärtner 2006).

Table 3 lists the different parameter values used in the numerical computations discussed in the following sections.

4.1.1. *Numerical homotopy method*

In general, the problem under consideration depends on several parameters. However, we will be interested in the influence of only one parameter on solutions, while the other parameters will be kept fixed. In the following section, the essential parameter is the height λ of a surface-mounted hump given by $S(X;\lambda)=\lambda S_0(X)$. Consequently, the numerical scheme and the resulting system of algebraic equations (4.13) will depend on λ as well, i.e. $\boldsymbol{F}(\boldsymbol{s};\lambda)=\boldsymbol{0}$. For small heights of the surface-mounted obstacle, the trivial solution of the interaction problem $\bar{U}\equiv V\equiv 0$ is found to be a reasonable initial guess to be used by the numerical equation solver and the solution is converged after several iteration steps. However, for larger λ, no convergence is observed and a numerical homotopy strategy (cf. e.g. Seydel & Hlavacek 1987; Stoer & Bulirsch 2002) is adopted. The sought after solution $\boldsymbol{s}_k$ of $\boldsymbol{F}(\boldsymbol{s};\lambda_k)=0$ is considered to be part of a family of solutions $\boldsymbol{s}(\lambda)$ of $\boldsymbol{F}(\boldsymbol{s};\lambda)=0$. From the solutions of two neighbouring problems $\boldsymbol{F}(\boldsymbol{s};\lambda_{i-1})=0$ and $\boldsymbol{F}(\boldsymbol{s};\lambda_i)=0$, an initial guess $\boldsymbol{s}_{i+1,est}$ for the solution of $\boldsymbol{F}(\boldsymbol{s};\lambda_{i+1})=0$ is constructed by tangential updating. If the initial guess is good enough to obtain a new solution for λ_{i+1}, the updating procedure described can be used to obtain a solution for λ_{i+2} and so forth until λ_k is obtained. The numerical homotopy method is supplemented by a continuation strategy to account for the observed sensitivity of solutions under parameter variation. To this end, the parameter λ is considered to be a variable itself and thus part of the solution. The system of equations $\boldsymbol{F}(\boldsymbol{s},\lambda)=0$ has to be supplemented by an additional equation $f(\boldsymbol{s},\lambda)=0$ in order to close the problem. The new problem

$$\mathbb{R}^{d+1}\ni\bar{\boldsymbol{F}}(\bar{\boldsymbol{s}})=\bar{\boldsymbol{F}}((\boldsymbol{s},\lambda)^{\mathrm{T}})=\begin{cases}\boldsymbol{F}(\boldsymbol{s},\lambda)=\boldsymbol{0},\\ f(\boldsymbol{s},\lambda)=0,\end{cases} \tag{4.14}$$

can be solved in the manner previously described. The phase condition $f(\boldsymbol{s}, \lambda) = 0$ is chosen as

$$f(\boldsymbol{s}, \lambda) = \|(\boldsymbol{s} - \boldsymbol{s}_i, \lambda - \lambda_i)\| - \Delta\lambda_i = 0. \tag{4.15}$$

The new solution $\bar{\boldsymbol{s}}_{i+1}$ lies on the surface of a sphere in the phase space with its centre at $\bar{\boldsymbol{s}}_i$ and a radius $\Delta\lambda_i$. Here $\Delta\lambda_i$ is adapted in each new step taking into account information of the convergence rate obtained in the previous homotopy step.

4.2. *Viscous Laval nozzle*

The oncoming subsonic, near-critical flow regime in a slender channel is affected by a small surface-mounted hump given by the relation, already written in the lower-deck scaling,

$$S(X) = \begin{cases} 0, & L_{\mathscr{N}} < |X|, \\ \dfrac{\lambda}{2}(1 + \cos(\pi X / L_{\mathscr{N}})), & |X| \leqslant L_{\mathscr{N}}. \end{cases} \tag{4.16}$$

The surface-mounted hump forms a small Laval nozzle of length $2L_{\mathscr{N}}$ located within a channel of constant cross-section, the dimensions of both the channel and the nozzle shall be consistent with the length scales proposed for a given Reynolds number regime in § 3.2. In particular, $\partial S(X)/\partial X = 0$ for $|X| > L_{\mathscr{N}}$ and the stationary solutions of the interaction problem have to satisfy the far upstream and downstream properties discussed in § 3.3. In the case of $\lambda > 0$, the nozzle consists of a converging, i.e. $S'(X) > 0$, for $X < 0$, and a diverging part, i.e. $S'(X) < 0$, for $X > 0$, which is the conventional design of Laval nozzles used to accelerate a regular working fluid, i.e. $\Gamma > 0$, from subsonic to supersonic flow conditions. In contrast, in order to convert the subsonic flow of a dense gas with $\Gamma < 0$ to the super sonic flow regime a nozzle is needed, which has a diverging upstream part and a converging downstream part, i.e. $\lambda < 0$ (cf. e.g. Kluwick 1993).

Sections 4.2.1 and 4.2.2 discuss the influence of the viscous–inviscid interaction on the resulting flow pattern for different heights λ in the case of a conventional type of fluid and a dense gas type of fluid, where $\Gamma < 0$ in the entire flow regime, respectively.

4.2.1. *Perfect-gas-like fluids: thermodynamic regions* $\Gamma > 0$

The working medium under consideration behaves as a conventional regular fluid, i.e. $\Gamma > 0$ in the entire flow regime of interest. Consequently, the parameter n, characterizing the thermodynamic properties of the working fluid, is of value 2. Since the oncoming flow is supposed to be subsonic, i.e. characterized by a positive value of the transonic similarity parameter $K > 0$, the negative mass-flux density perturbation $G_{[2]}$ (cf. (3.43)) takes on the quadratic functional form depicted in figure 5(*a*). Furthermore, we take $Q = 1$ in the interaction law (3.48); a discussion of the influence of Q on the flow regime is given at the end of this section. From an inspection of the expansion of the Mach number variation (3.49), it is evident that supersonic upper-deck flow is encountered for $P < -1$ and sonic flow conditions are reached for $P = -1$, where $G_{[2]}$ becomes extremal.

Recalling the discussion of the far upstream and downstream properties of possible solutions in § 3.3, we find that the flow upstream of the nozzle, i.e. for $X < -L_{\mathscr{N}}$, is unaffected by the presence of the surface-mounted hump, because under subsonic flow conditions no non-trivial eigensolutions exist, which could contribute to a free-interacting part of the solution. Hence, the flow in the interaction region for $X < -L_{\mathscr{N}}$ is identical to the oncoming flow conditions $(P, A) = (0, 0)$. Once the nozzle is reached,

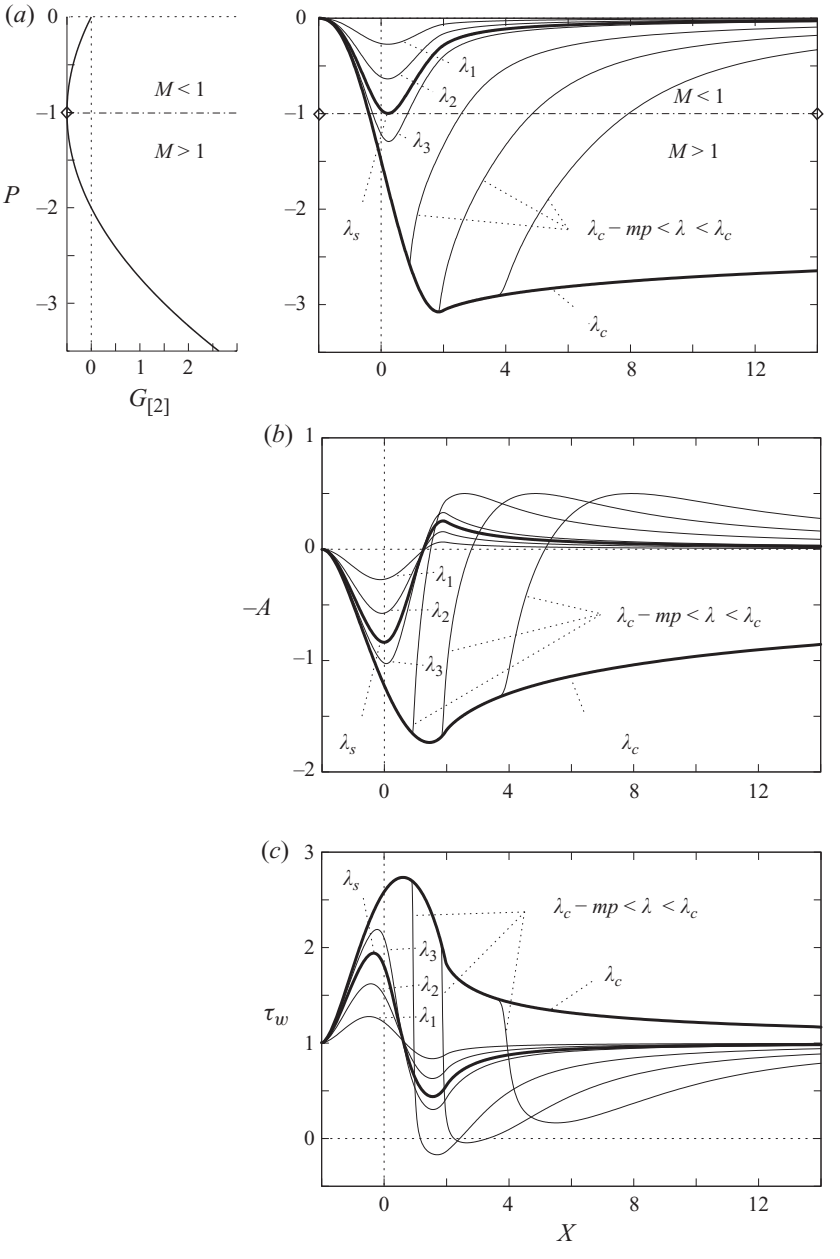

FIGURE 5. Plot of (*a*) the *P*-, (*b*) $-A$- and (*c*) τ_w $(= \partial U/\partial Y|_{Y=0})$-distributions for various heights λ of the surface-mounted hump of length $L_{\mathcal{N}} = 2$ for $n = 2$, $\Gamma > 0$ and $Q = 1$. The numerical values for λ are $\lambda_1 = 0.5$, $\lambda_2 = 1.0$ and $\lambda_3 = 1.5$. A sonic state, indicated by $\diamond$, is first encountered for $\lambda_s \approx 1.335$. Transition from subsonic to supersonic flow for $\lambda_c = 1.60512\ldots$, for $\lambda \to \lambda_c-$ pseudo-shocks form, leading to a smooth transition from supersonic to subsonic flow; *mp* denotes machine precision. For $\lambda > \lambda_c$, no steady solutions exist.

the interaction process is triggered and the flow deviates from undisturbed oncoming flow conditions. Naturally, the resulting flow pattern in the nozzle depends on the chosen properties of the nozzle and can only be obtained by numerical solutions, in general. Far downstream of the nozzle, however, the asymptotic form of the solutions

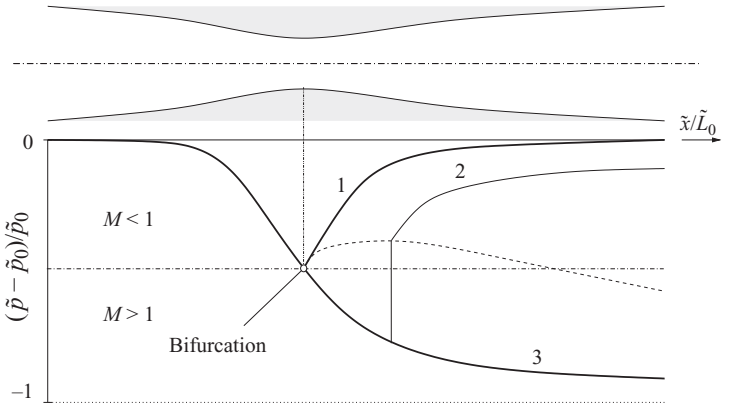

FIGURE 6. Sketch of the pressure distribution in an ideal Laval nozzle according to classical theory (inviscid one-dimensional, non-interacting flow, perfect gas).

again is known and has to satisfy (3.51) and (3.53). Obviously, there exist two possible flow regimes far downstream of the interaction region, namely $(P_\infty, A_\infty) = (0, 0)$ and $(P_\infty, A_\infty) = (-2, 0)$, which are approached in the weak algebraic manner indicated by (3.51) and (3.53). The first state, which is identical to the flow conditions in the oncoming flow, indicates subsonic, whereas the second state indicates supersonic downstream flow conditions.

In order to understand the observed multivaluedness of the far downstream state, one has to give attention to the evolution of the flow in the nozzle part of the channel. Therefore, turning now to numerical solutions, we consider a nozzle of a shape given by (4.16) with $L_{\mathscr{N}} = 2$. Figure 5(*a–c*) shows the numerical results for the perturbations of the pressure P (figure 5*a*), the negative displacement thickness evoked by the viscous lower-deck reaction $-A$ (figure 5*b*) and the wall shear stress $\tau_w = \partial U/\partial Y|_{Y=0}$ (figure 5*c*). For small heights of the surface mounted hump, cf. the distribution of the pressure for $\lambda_1 = 0.5$ and $\lambda_2 = 1.0$ in figure 5(*a*), the upper-deck flow remains subsonic in the entire interaction region. This behaviour is very much in line with the well-known behaviour of the perfect-gas-like flow through a Laval nozzle of a minimal throat area, which is larger than the critical minimal throat area, according to the classical, purely inviscid and one-dimensional theory; see e.g. Oswatitsch (1956) and the sketch in figure 6. Initially, the oncoming upper-deck flow is accelerated in the converging part of the nozzle indicated by the decreasing pressure. However, unlike classical theory, where the flow decelerates immediately after traversing the minimum throat area, which is located at $X = 0$, the interacting core-region flow is accelerating right into the first part of the diverging section of the nozzle, before, finally, it is decelerated back to the undisturbed subsonic downstream flow state $(P, A) = (0, 0)$. The cause of the observed deviation from classical behaviour is that the interacting boundary layers themselves are forming a 'viscous' Laval nozzle which adds up to the geometrical (solid) shape S of the nozzle. Thus, the effective crossflow reduction felt by the upper-deck flow, which is a result from the boundary layer displacement exerted on the core-region flow (cf. figure 3), consists of the 'geometric' contribution S and a purely viscous contribution $-A$, shown in figure 5(*b*), generated by the lower-deck reaction to the induced pressure variation in the upper deck. Both effects contribute to the perturbation of the boundary layer displacement in the interaction region $-A_1$, which is expressed by the relation (3.34) of Prandtl's transposition theorem, which is

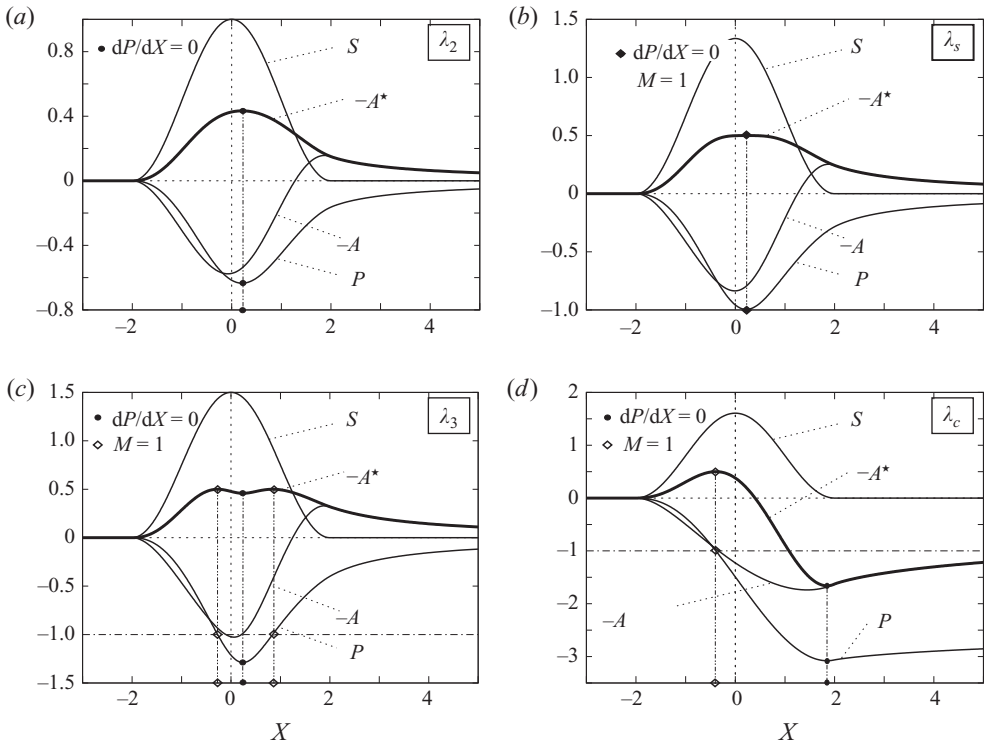

FIGURE 7. Plot of the P-, $-A$-, S- and $-A^\star = -A + S$-distributions for various heights λ of the surface-mounted hump of length $L_{\mathscr{N}} = 2$ for $n = 2$, $\Gamma > 0$ and $Q = 1$. (*a*) $\lambda_2 = 1.0$, (*b*) $\lambda_s \approx 1.335$, (*c*) $\lambda_3 = 1.5$ and (*d*) $\lambda_c = 1.60512\ldots$.

given here in canonical form

$$-A^\star := -R_0(0)^{1/2} U_0'(0) |2\bar{\Gamma}/K|^{1/2} A_1 = -A + S \tag{4.17}$$

for the overall perturbation of the negative displacement thickness $-A^\star$. Insertion into the interaction law (3.42) for steady flow, which governs the core-region flow, yields the alternative form of the interaction law

$$G'_{[n]}(P; K, \Gamma_{-\infty}, \Lambda_{-\infty}, N_{-\infty}) \frac{\mathrm{d}P}{\mathrm{d}X} = Q \frac{\mathrm{d}A^\star}{\mathrm{d}X} = Q \frac{\mathrm{d}}{\mathrm{d}X}(A - S). \tag{4.18}$$

Figure 7(*a*) once again shows the distribution of P for the case of $\lambda_2 = 1.0$, but now together with the distributions of S, $-A$ and $-A^\star$. The compressible inviscid upper-deck flow is accelerated as long as $\mathrm{d}P/\mathrm{d}X < 0$. Initially, the incompressible lower-deck flow is accelerated as well and by continuity arguments this results in a thinning of the boundary layer indicated by $\mathrm{d}(-A)/\mathrm{d}X < 0$ leading to $-A < 0$. Therefore, the contribution of the surface-mounted hump S on the displacement effect is reduced by A and the point of deceleration of the upper-deck flow ($\mathrm{d}P/\mathrm{d}X = 0$) is delayed into the diverging part of the nozzle. In the classical picture of a non-interacting inviscid flow, a nozzle would have to have a shape given by $-A^\star$ in order to obtain the same pressure distribution as observed in the case of an interacting flow through a nozzle of shape S. In fact, the interacting boundary layer can be seen to form a 'viscous' nozzle of shape $-A^\star$ for the inviscid core-region flow in the upper deck, which, however,

because of the interaction has to adapt to and, at the same time, interact with the inviscid channel core flow. Interestingly, the deceleration of the upper-deck flow is preceded by a deceleration of the boundary layer flow (indicated by a thickening of the boundary layer $\mathrm{d}(-A)/\mathrm{d}X > 0$), so that the resulting effective displacement $-A^\star$ has an extremum at P_{min}, the beginning of the retardation of the upper-deck flow. The location of the minimal effective throat area of this viscous nozzle now corresponds with the minimum of the pressure distribution P_{min}, as one would have guessed by application of the classical Laval nozzle theory and which follows from (4.18) taking into account that $G'_{[2]}(P_{min}) \neq 0$ in figure 7(*a*).

If the height of the surface-mounted hump is increased successively to $\lambda_s \approx 1.335$, the minimum of the pressure distribution approaches $P_s = -1$, eventually. At this point, sonic flow conditions are obtained for the first time in the nozzle. In the classical Laval nozzle theory, this is the limiting case of the critical minimal throat area and no steady solutions exist in the case of a further reduction of the throat area, i.e. increase of the surface-mounted hump. Moreover, the sonic state located at the minimal throat area would correspond to a bifurcation point in the pressure distribution branching two solutions. One solution branch would correspond to a subsonic decelerating flow regime, and the other would correspond to a supersonic accelerating flow; cf. branch 1 and branch 3 in figure 6, respectively. The numerical results for the pressure distribution in figure 5(*a*) clearly show that the bifurcation point for λ_s is eliminated under the action of the viscous–inviscid interaction, which in a sense regularizes the idealization of a purely inviscid flow required by the classical picture. Only one branch of the former two solution branches remains accessible, which leads to a reversion to the subsonic flow regime. Interestingly enough, the height of the surface-mounted hump can be increased above λ_s, cf. the case $\lambda_3 = 1.5$ in figure 5(*a*). The pressure distribution for λ_3 indicates that the upper-deck flow is accelerated first to supersonic, but afterwards *smoothly* decelerated to subsonic conditions again. Such a solution has no counterpart in the classical Laval nozzle theory. Figure 7(*c*) reveals that the interacting boundary layers are forming a viscous nozzle consisting now of two throats and one anti-throat and that the *local* supersonic flow regime is confined between the two throats. The two sonic states are located at the minima of the two viscous throats and the minimum of the pressure distribution is located at the maximum of the viscous anti-throat. This immediately follows from (4.18), since in the case of an extremum of $A^\star(X)$, i.e $\mathrm{d}A^\star/\mathrm{d}X = 0$, $P(X)$ has to become extremal too, i.e. $\mathrm{d}P/\mathrm{d}X = 0$, if $M \neq 1$, and thus $G'_{[2]} \neq 0$. Only at a sonic state, i.e. $G'_{[2]} = 0$, it is possible to pass the sonic state and to enter a different flow regime (from subsonic to supersonic or vice versa), since only then $\mathrm{d}P/\mathrm{d}X \neq 0$ in accordance with (4.18).

As expected, the height of the surface-mounted hump cannot be increased indefinitely. The numerical investigation indicates the existence of a critical value $\lambda_c \approx 1.60512$ above which no steady solutions can be found. Very much like the case of an ideal Laval nozzle according to the classical theory (cf. the solution branch 3 in figure 6), the solution for λ_c is just the solution, which leads to a transition from the subsonic into the supersonic regime with $P_\infty = -2$. In this limiting case, the viscous nozzle of shape $-A^\star$ in figure 7(*d*) is found to form a nozzle, which now consists of only one throat and one anti-throat, leading to a shock-free acceleration of the upper-deck flow into the supersonic flow regime. Quite in contrast to the classical Laval nozzle theory (cf. figure 6), the supersonic downstream pressure state is not approached in a monotonous way (cf. figure 5*a*), but rather exhibits a pressure minimum within the nozzle because of viscous–inviscid interactions.

Moreover, with λ approaching λ_c from below, the region around the location of the minima in the corresponding pressure distributions is almost forming a cusp (cf. figure 5*a*). From a numerical point of view, such solutions are indistinguishable to the machine precision mp, i.e. $0 < \lambda_c - \lambda < mp$, from the solution for λ_c as long as the flow in the nozzle is accelerated, i.e. $\mathrm{d}P/\mathrm{d}X < 0$ in figure 5(*a*). Then, the solutions seem to branch from the solution for λ_c, leading to a relatively rapid transition from super- to subsonic flow conditions. Interestingly enough, there exists a classical counterpart which is depicted in figure 6, cf. branch 2. A normal shock in the diverging part of the nozzle leads to the transition from supersonic to subsonic flow, the position of the shock depends on the outflow condition at the nozzle exit. However, taking into account the results presented in Kluwick & Meyer (2010), it follows that such a weak normal shock is smoothed out by the mechanism of viscous–inviscid regularization because of strong shock-boundary layer interactions taking place in slender channels, and the shock discontinuity resolves into a pseudo-shock. By means of the numerical homotopy continuation method (cf. §4.1.1), an infinite number of solutions can be found for $0 < \lambda_c - \lambda < mp$ (cf. figure 5). The position of the pseudo-shock is moved successively further downstream until it eventually leaves the physical domain, resulting in the limiting case for $\lambda = \lambda_c$. The flow in such a regime, in analogy to the classical Laval nozzle theory, can be considered to be nearly choked. Eventually, the strength of such a pseudo-shock forming in the choked flow regime is large enough to force the lower-deck flow to separate (cf. figure 5*c*). Such a phenomenon is well known and frequently encountered in technical transonic diffusers and is very susceptible to self-sustained shock oscillations (cf. e.g. Matsuo, Miyazato & Kim 1999).

Whether flow separation is caused by pseudo-shocks in the diffuser part of the nozzle depends on several parameters, amongst them the chosen length of the nozzle $L_{\mathscr{N}}$ and the parameter Q governing the coupling between the lower- and upper-deck flows. This is exemplified by figure 8. Figure 8(*a*) shows two pseudo-shocks and the solution for λ_c for different values of the parameter Q. Apart from the different critical heights of the surface-mounted hump necessary for different values of Q, the shape of the nozzle S remains unchanged with respect to the already discussed situation of $Q = 1$, which is depicted by the bold solid lines in figure 8(*a*). In particular, the length of the surface-mounted hump $L_{\mathscr{N}} = 2$. A reduction of Q, and linked to it a reduction of the strength of the regularizing influence, the interaction process can be achieved for instance by increasing the height of the channel H_{01} while keeping the inflow conditions fixed at the same time (cf. (3.47)). The minimum of the pressure distribution in the nozzle, which, as pointed out before, is the direct consequence of the viscous–inviscid interaction mechanism, decreases with increasing values of Q, i.e. with increasing strength of the coupling between the interacting boundary layer flow and the upper deck. Consequently, the strength of a pseudo-shock in the diffuser part is increased and the pseudo-shock initiated approximately between $X = 0$ and $X = 2$ causes flow separation in the boundary layers for all depicted values of Q. On the other hand, from the results presented in Kluwick & Meyer (2010), it is evident that the steepness of the shock profiles and thus the likelihood to encounter flow separation in compressive pseudo-shocks of similar strength increases with decreasing values of Q. Thus, considering the pseudo-shock solutions starting at approximately between $X = 2$ and $X = 4$, i.e. outside the nozzle, only the pseudo-shock corresponding to the lowest value of $Q = 0.7$ is found to cause flow separation. Note that the calculated values of the critical surface contour λ_c for the different values of Q do not vary monotonically with Q. This exemplifies the significance of the strong interaction between the boundary layer flow and the flow regime in the inviscid core in slender

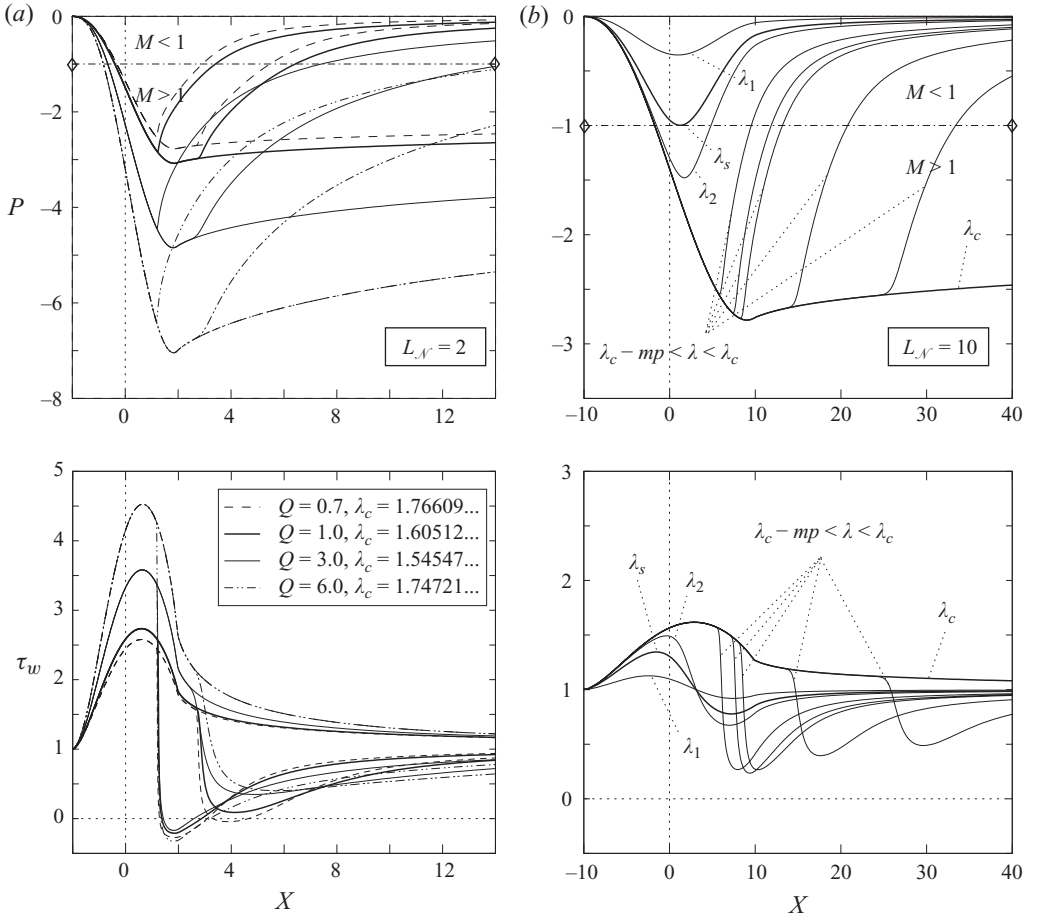

FIGURE 8. (*a*) Plot of the P- and τ_w $(=\partial U/\partial Y|_{Y=0})$-distributions for various values of the parameter Q in the choked flow regime of a surface-mounted hump of length $L_{\mathscr{N}}=2$ for $\lambda\to\lambda_c-$. (*b*) Plot of the P- and τ_w-distributions for various heights λ of the surface-mounted hump of length $L_{\mathscr{N}}=10$ and $Q=1$. The numerical values for λ are $\lambda_1=0.5$ and $\lambda_2=1.5$. A sonic state, indicated by $\diamond$, is first encountered for $\lambda_s\approx 1.075$. Transition from subsonic to supersonic flow for $\lambda_c=1.28210\ldots$, for $\lambda\to\lambda_c-$ pseudo-shocks form; *mp* denotes machine precision.

nozzles, since, as discussed before, the geometric shape of the nozzle alone is no longer responsible for the transition from subsonic to supersonic, but has to be considered together with the boundary layer displacement.

If $L_{\mathscr{N}}$ is increased for a given shape of a nozzle and a given value of Q, then flow separation can be avoided for all pseudo-shock solutions (cf. figure 8*b*). Figure 8(*b*) shows various pressure distributions for a surface-mounted hump of length $L_{\mathscr{N}}=10$ for $Q=1$. The strength of the pseudo-shocks that form is decreased in comparison to the case of $L_{\mathscr{N}}=2$ (cf. figures 8*a* and 5*a*), which is sufficient to avoid flow separation in the case of a nozzle with $L_{\mathscr{N}}=10$ for $Q=1$, in general.

In conclusion, note that flow separation can also be obtained by a proper design of the nozzle diffuser part, so that flow separation would be caused by the adverse pressure gradient developing in the subsonic flow regime downstream of the pseudo-shock. Instead of the shock-induced flow separation caused by a pseudo-shock, we

then would have to deal with pressure-gradient-induced flow separation caused by a sufficient steepness of the diffuser part in the nozzle. However, since these observations do not add much to the discussion already presented, we state these facts for the sake of completeness, but refrain from a more detailed discussion.

4.2.2. *Real gas effects: thermodynamic regions* $\Gamma < 0$

The working medium under consideration is taken to be a real gas in the dense gas regime having $\Gamma < 0$ in the entire flow region of interest. Thus, as before, the parameter n is of value 2 and the negative mass-flux density perturbation $G_{[2]}$ (cf. (3.43)) again takes on a quadratic functional form. Since the oncoming flow is supposed to be subsonic once again, the transonic similarity parameter $K > 0$ has to be positive. The sonic state, however, is now attained at $P = 1$ and the supersonic flow regime is accessed for $P > 1$. As before, the interacting flow for $X < -L_{\mathscr{N}}$ is given by $(P, A) = (0, 0)$, since under subsonic flow conditions no upstream influence of the surface-mounted hump can develop (cf. the discussion in § 3.3). The two possible flow regimes far downstream of the interaction region are $(P_\infty, A_\infty) = (0, 0)$ (subsonic) and $(P_\infty, A_\infty) = (2, 0)$ (supersonic), which are approached in the weak algebraic manner indicated by (3.51) and (3.53). The appropriate nozzle to obtain supersonic flow conditions (note that in a dense gas with $\Gamma < 0$, the flow has to decelerate in order to enter the sonic flow regime) has to consist of one anti-throat rather than one throat as in § 4.2.1. Consequently, we chose the height of the surface-mounted hump λ governing the nozzle geometry in relation (4.16) to be of negative values.

Figure 9 illustrates the influence of the height of the surface-mounted hump λ on the distributions of the corresponding induced pressure P, the effective boundary-layer displacement $-A^\star$ (cf. (4.17)), and the wall shear stress $\tau_w = \partial U/\partial Y|_{Y=0}$ in the interaction region for two different values of $L_{\mathscr{N}}$. The results with $L_{\mathscr{N}} = 10$ are plotted in the left column of figure 9 and the results with $L_{\mathscr{N}} = 15$ in the right. Different solutions in the charts of figure 9 correspond to different heights λ_α; the numerical values of λ_α are defined by their index α.

The qualitative behaviour of the solutions obtained for the various values of λ in figure 9 is found to be very similar to that discussed in the previous section, aside from the reversed nozzle shape and the indicated rarefactive nature of pseudo-shocks. The shape of the viscous nozzle $-A^\star$, which is formed by the boundary layers interacting with the induced pressure perturbations in the core region (cf. figure 9*b*), consists either of one anti-throat (subsonic), of two anti-throats confining a supersonic regime and one throat located at the maximum of the pressure distribution (supersonic pocket), or of one anti-throat and one throat (ideal Laval nozzle). Since the admissible type of shocks in dense gases with $\Gamma < 0$ are rarefaction shocks (Kluwick 1993), pressure-induced flow separation is avoided, in general. Because of the favourable influence of a negative pressure gradient in the resulting pseudo-shock profile, the boundary layer flow remains firmly attached; cf. the positive peaks in the wall-shear distribution in figure 9(*c*). By an inspection of the wall-shear distributions in the case of $L_{\mathscr{N}} = 10$, for which no flow separation has been observed in the case of $\Gamma > 0$ (cf. figure 8*b*), it becomes evident that the risk of flow separation in Laval nozzles is by no means eliminated by the use of dense gases, since transition from subsonic to supersonic flow is caused by a suitable deceleration of the flow and a net increase of the Mach number is achieved by the even stronger decrease of the speed of sound. Consequently, the boundary layer flow is decelerated initially when subjected to the subsonic retarded core-region flow and, thus, the risk of flow separation is shifted from the supersonic flow regime (shock-induced flow separation) into the subsonic flow regime of the

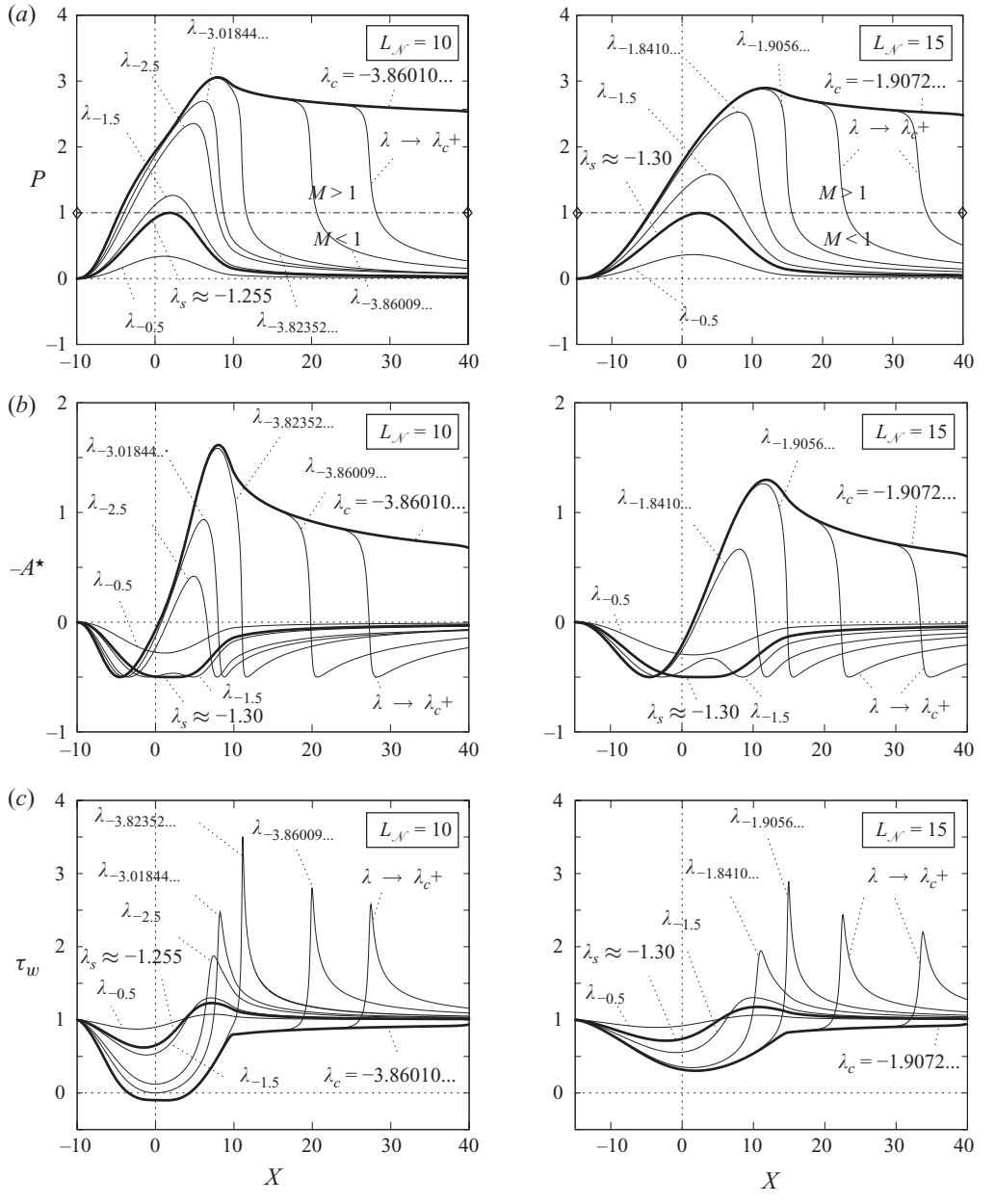

FIGURE 9. Plot of (*a*) the P-, (*b*) $-A^\star$- and (*c*) τ_w ($= \partial U/\partial Y|_{Y=0}$)-distributions for various heights λ of the surface-mounted hump with $L_{\mathscr{N}} = 10$ (left) and $L_{\mathscr{N}} = 15$ (right) and $Q = 1$ for a dense gas characterized by $n = 2$ ($\Gamma < 0$). The numerical values for λ in the figures are given by their indices. A sonic state, indicated by $\diamond$, is first encountered for λ_s. Transition from subsonic to supersonic flow for λ_c; *mp* denotes machine precision.

diffuser part of the nozzle (pressure-gradient-induced flow separation). Naturally, the tendency to cause flow separation should decrease for nozzles of greater length $L_{\mathscr{N}}$; cf. the case $L_{\mathscr{N}} = 15$ in figure 9, where the boundary layer flow remains attached for all possible values of λ. Interestingly, in the case of a pressure-gradient-induced flow

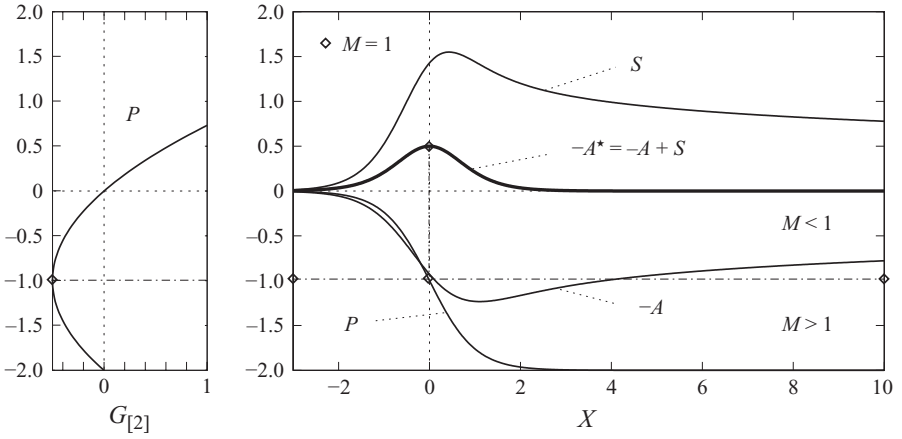

FIGURE 10. Inverse design of a nozzle for perfect-gas-like fluids ($n = 2$); $Q = 1$.

separation taking place, λ can be decreased significantly below the values possible in the case without separation. Even so, the values for λ_s, where sonic flow conditions are encountered in the nozzle for the first time, are of comparable numeric values in both cases. Furthermore, flow separation leads to a slight depression in the pressure distribution, where the pressure rise achieved in the separation region is comparably small as λ is pushed further towards the critical value λ_c. Consequently, the maximal pressure values observed in the nozzle of $L_{\mathcal{N}} = 10$ and $L_{\mathcal{N}} = 15$ are of about 3 in both cases (cf. figure 9*a*), whereas the maximal boundary displacement $-A^\star$ and the wall shear stress are significantly higher in the case $L_{\mathcal{N}} = 10$, where flow separation occurs, than those in the case $L_{\mathcal{N}} = 15$ without any separation region (cf. figures 9*b* and 9*c*). Quite in contrast to the behaviour found for a regular fluid in § 4.2.1, the formation of pseudo-shocks is eased somewhat, so that they are already present for values of λ well below λ_c (and even more so, when the pressure-gradient-induced flow separation precedes the pseudo-shock). Experiments in the dense gas regime may possibly benefit from this fact, since it should facilitate the adoption of a proper maximal flow cross-section in a nozzle in order to obtain a specific choice of a pseudo-shock solution suitable for the experimental detection.

4.3. *Inverse problem: Laval nozzle design*

From a practical viewpoint, it seems more natural to ask for the appropriate nozzle shape in order to generate a certain desired pressure distribution, which e.g. ensures a smooth conversion of the subsonic oncoming flow into the supersonic downstream flow conditions. The changes required in the numerical scheme are straightforward, instead of $S(X)$ we simply prescribe $P(X)$ and $S(X)$ is considered to be unknown in advance. The numerical results for the desired pressure distribution of a regular fluid given by the functional form

$$P(X) = P_\infty(\tanh(X) + 1)/2, \tag{4.19}$$

with the chosen downstream pressure $P_\infty = -2$, are plotted in figure 10. It is evident that a nozzle forming the desired pressure distribution has to have a slowly diverging part reaching far downstream. The exponential approach of the downstream pressure P_∞, which is desired by relation (4.19), forces the same exponential behaviour of the effective boundary layer displacement $-A^\star$ according to (4.18). And, consequently,

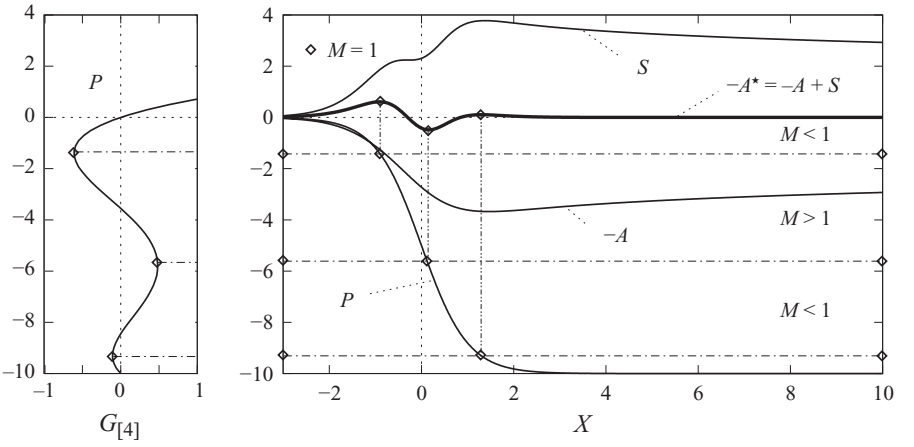

FIGURE 11. Inverse design of a Laval nozzle for dense gas ($n = 4$, $K > 0$, $\Gamma_{-\infty} > 0$, $\Lambda_{-\infty} = 0.44$, $N_{-\infty} = 0.08$); $Q = 1$.

the weak algebraic decay of $-A$ shown in figure 10 has to be balanced by the weak algebraic decay of the solid nozzle shape S.

So far, the discussion has been restricted to regular fluids or dense gases, where it has been assumed that the flow states within the nozzle never leave the dense gas regime, i.e. $\Gamma < 0$ for all possible flow situations encountered. If, however, the operation mode of the nozzle is located close to the transition line $\Gamma = 0$, we have to consider dense gases exhibiting mixed nonlinearity, i.e. the fundamental derivative (1.1) is likely to change its sign as well. The conversion of the working media from subsonic to supersonic flow cannot be accomplished by means of a nozzle consisting out of one single throat in that case (cf. Kluwick 1993). Rather, a combination of throats and anti-throats has to be used. In such a case, the inverse design of a Laval nozzle is most useful, since the procedure to increase the height of a nozzle of otherwise given shape until a critical value of the nozzle height is obtained will not result in a transition from subsonic to supersonic flow conditions, in general. Figure 11 shows numerical results for the instructive case of a dense gas flow in which the unperturbed state upstream of the interaction region is characterized by $\Gamma_{-\infty} > 0$, $\Lambda_{-\infty} = 0.44$ and $N_{-\infty} = 0.08$. The actual numerical values used in figure 11 are chosen in such a way that they result in a mass-flux density with three well-separated sonic states. Inspection of the mass-flux density $G_{[4]}$ depicted in figure 11 reveals the existence of three sonic states separating four Mach number regimes. In the actual case, the fluid is accelerated from subsonic conditions with $(P, A) = (0, 0)$ to supersonic downstream conditions with $(P_\infty, A_\infty) = (-10, 0)$ traversing first a supersonic region and a successive subsonic region before entering the desired second supersonic flow regime. The required shape of the nozzle is shown in figure 11 together with the effective shape of the viscous nozzle $-A^\star$, which indeed exhibits the two throats and the one throat as indicated earlier. The first throat is necessary to accelerate the flow from subsonic to supersonic, in the following anti-throat it is accelerated further to subsonic, and in the second anti-throat it is finally forced into the second supersonic flow regime.

5. Summary and conclusions

The problem of viscous–inviscid interactions in internal, transonic, single phase and two-dimensional high-Reynolds-number flows of regular and dense gases through

narrow channels has been consistently generalized to deal with small Laval nozzles located in a channel of an otherwise constant cross-section. The resulting problem can be described in the framework of the triple-deck theory. The channel is required to be so narrow that the interacting core-region flow becomes one-dimensional to leading order, the interacting core region is then represented by a single upper deck which is shared by the two interacting boundary layers at the lower and upper channel walls. The resulting model equations have been applied to study the conversion of subsonic to supersonic flows for fluids of general type. Because of the nature of the asymptotic analysis employed here, the emphasis has been laid on identifying and describing the underlying physical agencies at work.

The first part of the discussion of the resulting steady flow field through nozzles of different minimum cross-sections, but of otherwise similar shape, focuses on the case of a regular fluid for example an ideal gas. The nozzle is of conventional shape in the sense that it consists of a converging part followed by a diverging part. Because of the regularizing effect of the viscous–inviscid interactions, the occurrence of a single sonic state in the inviscid core-region flow no longer corresponds to a bifurcation point, as is the case in the classical inviscid one-dimensional Laval nozzle theory. The numerical results show that the purely subsonic solution remains the only possible solution and no supersonic branch bifurcates at the sonic state. Moreover, the sonic point moves slightly downstream of the location of the minimum throat area of the nozzle. A quite similar behaviour concerning the location of the sonic point has been reported in computational fluid dynamics (CFD) results for transonic flow through micro nozzles (see for example Hao *et al.* 2005), and for nozzle flow at moderately high Reynolds numbers where the viscous effects are important in the whole flow field (Williams III 1963). Unlike classical theory, at this point the minimum throat area is still larger than the critical minimum cross-section, so that there is the potential in interacting flows to further increase the geometrical constriction of the core-flow region. The explanation of such a behaviour is the 'freedom' of the interacting boundary layers to form a 'viscous' nozzle, which adapts and at the same time interacts with the inviscid channel core flow similar to the shock-regularizing mechanism of viscous–inviscid interactions discussed in Kluwick & Meyer (2010). Therefore, the effective shape of the viscous nozzle is now a combination of the purely viscous lower-deck response and the geometrical nozzle shape. The minimum cross-section of the nozzle cannot be reduced without bounds. In the vicinity of the minimal critical cross-section, which leads to a smooth transition from subsonic to supersonic conditions, pseudo-compression shock solutions start to form in the diffuser part of the nozzle, leading to a rapid transition of the supersonic flow to subsonic conditions. The pseudo-shock has been found to move successively downstream when the minimum cross-section is approached. This flow regime has been denoted as nearly chocked flow, in analogy to the classical Laval nozzle theory. Eventually, depending on the shape of the nozzle and the strength of the coupling between the lower and upper-deck flows represented by the parameter Q in (3.42), the pseudo-shock is strong enough to force flow separation to occur. Preliminary results obtained by a linear stability analysis for steady solutions show that separation is linked to the loss of stability of the steady solutions. The emphasis of this work is to establish how this is related to the well-known phenomenon of self-sustained shock wave oscillations in transonic diffusers (cf. e.g. Matsuo *et al.* 1999).

Turning to the analogous problem for dense gases where the fundamental derivative $\Gamma < 0$ is negative in the entire flow regime of interest, the proper shape of a nozzle to convert the oncoming subsonic flow to supersonic conditions consists now of a

diverging part followed by a converging part and the obtained pseudo-shock solutions correspond to rarefaction shocks rather than to compression shocks (cf. e.g. Kluwick 1993). Because of the rarefactive nature of the pseudo-shocks, no risk of the shock-induced flow separation is encountered here. However, the numerical solutions reveal a tendency to exhibit pressure-gradient-induced flow separation in the preceding subsonic diffuser part of the nozzle, again depending on the shape of the nozzle under consideration. In comparison with the behaviour found for a regular fluid, the formation of pseudo-shocks is eased in general, so that they are already present for nozzles with a maximum flow cross-section well below the critical limiting situation of an ideal Laval nozzle resulting in a smooth transition to supersonic downstream flow conditions (and even more so, when the pressure-gradient-induced flow separation precedes the pseudo-shock). Experiments in the dense gas regime may possibly benefit from this situation, since it should facilitate the adoption of a proper maximal flow cross-section in a nozzle in order to obtain a specific choice of a pseudo-shock solution suitable for the experimental detection.

The formulation of the problem presented so far, that is to say, prescribing the shape of the nozzle, has turned out to be quite revealing in the discussion of the family of solutions to be encountered; however, it allows limited control over the obtained pressure distribution. Moreover, it is quite demanding to obtain a smooth transition from subsonic to supersonic flow conditions of a dense gas undergoing a change of the sign of the fundamental derivative Γ in the flow field by simply prescribing a fixed nozzle shape. Therefore, the appropriate problem formulation is in terms of an inverse design of Laval nozzle, where the desired pressure distribution is given at the beginning and the corresponding unknown shape of the Laval nozzle is calculated in the end.

This work has been financed by the Austrian Science Fund in the framework of the WK Differential Equations. Additionally, G.M. thanks R. Szeywerth for his help with the implementation of the PARDISO routine.

REFERENCES

Brown, B. P. & Argrow, B. M. 2000 Application of Bethe–Zel'dovich–Thompson fluids in organic Rankine cycle engines. *J. Propul. Power* **16** (6), 1118–1124.

Cinnella, P. & Congedo, P. M. 2007 Inviscid and viscous aerodynamics of dense gases. *J. Fluid Mech.* **580**, 179–217.

Cramer, M. S. 1991 Nonclassical dynamics of classical gases. In *Nonlinear Waves in Real Fluids*. CISM Courses and Lectures No. 315 (ed. A. Kluwick), pp. 91–145. Springer.

Fergason, S. H., Ho, T. L., Argrow, B. M. & Emanuel, G. 2001 Theory for producing a single-phase shock wave. *J. Fluid Mech.* **445**, 37–54.

Guardone, A., Zamfirescu, C. & Colonna, P. 2010 Maximum intensity of rarefaction shock waves for dense gases. *J. Fluid Mech.* **642**, 127–146.

Hao, P.-F., Ding, Y.-T., Yao, Z.-H., Feng, H. & Zhu, K.-Q. 2005 Size effect on gas flow in micro nozzles. *J. Micromech. Microengng* **15**, 2069–2073.

Kluwick, A. 1993 Transonic nozzle flow of dense gases. *J. Fluid Mech.* **247**, 661–688.

Kluwick, A. 1998 Interacting laminar and turbulent boundary layers. In *Recent Advances in Boundary Layer Theory*. CISM Courses and Lectures No. 390 (ed. A. Kluwick), pp. 231–330. Springer.

Kluwick, A. 2004 Internal flows of dense gases. *Acta Mechanica* **196**, 123–143.

Kluwick, A. 2009 Transonic flows in narrow channels. *J. Therm. Sci.* (invited) **18** (2), 99–108. Dedicated to Prof. Dr.-Ing. Dr.techn. E.h. Jürgen Zierep on the occasion of his 80th birthday.

Kluwick, A., Exner, A., Cox, E. A. & Grinschgl, Ch. 2010 On the internal structure of weakly nonlinear bores in laminar high Reynolds number flow. *Acta Mechanica* **210** (1–2), 135–157.

Kluwick, A. & Meyer, G. 2010 Shock regularization in dense gases by viscous–inviscid interactions. *J. Fluid Mech.* **644**, 473–507.

Lighthill, M. J. 2000 Upstream influence in boundary layers 45 years ago. *Phil. Trans. R. Soc.: Math. Phys. Engng Sci.* **358** (1777), 3047–3062.

Matsuo, K., Miyazato, Y. & Kim, H. 1999 Shock train and pseudo-shock phenomena in internal gas flows. *Prog. Aerosp. Sci.* **35** (1), 33–100.

Oswatitsch, K. 1952 *Gas Dynamics*. Academic Press.

Oswatitsch, K. & Wieghardt, K. 1946 Theoretical investigations on steady potential flows and boundary layers at high speed. *Rep.* 10378. Aeronaut. Res. Council, London.

Powell, M. 1970 A hybrid method for nonlinear equations. In *Numerical Methods for Nonlinear Algebraic Equations* (ed. P. Rabinowitz), chap. 6, pp. 115–161. Gordon and Breach.

Prandtl, L. 1938 Zur Berechnung der Grenzschichten. *Z. Angew. Math. Mech.* **18**, 77–82.

Reyhner, T. A. & Flügge-Lotz, I. 1968 Interaction of a shock wave with a laminar boundary layer. *Intl J. Nonlinear Mech.* **3**, 173–199.

Schenk, O. & Gärtner, K. 2004 Solving unsymmetric sparse systems of linear equations with PARDISO. *J. Future Gener. Comput. Syst.* **20** (3), 475–487.

Schenk, O. & Gärtner, K. 2006 On fast factorization pivoting methods for symmetric indefinite systems. *Elec. Trans. Numer. Anal.* **23**, 158–179.

Schenk, O., Gärtner, K. & Fichtner, W. 2000 Efficient sparse LU factorisation with left–right looking strategy on shared multiprocessors. *BIT* **40** (1), 158–176.

Seydel, R. & Hlavacek, V. 1987 Role of continuation in engineering analysis. *Chem. Engng Sci.* **42** (6), 1281–1295.

Stewartson, K. 1974 Multistructured boundary layers on flat plates and related bodies. *Adv. Appl. Mech.* **14**, 145–239.

Stewartson, K. 1981 D'Alembert's paradox. *SIAM Rev.* **23** (3), 308–343.

Stoer, J. & Bulirsch, R. 2002 *Introduction to Numerical Analysis,* 3rd edn. Texts in Applied Mathematics, vol. 12. Springer.

Williams III, J. C. 1963 Viscous compressible and incompressible flow in slender channels. *AAIA J.* **1** (1), 186–195.